State of Health Forecasting of Lithium-Ion Batteries operated in a Battery Electric Vehicle Fleet

Friedrich von Bülow[a*], Markus Wassermann[a], and Tobias Meisen[b]

[a] *Volkswagen AG, Berliner Ring 2, 38440 Wolfsburg, Germany*

[b] *Institute of Technologies and Management of the Digital Transformation, University of Wuppertal, Rainer-Gruenter-Str. 21, 42119, Wuppertal, Germany*

Abstract

Most existing methods for battery state of health (SOH) forecasting have been applied to battery cell data from laboratory operation for training and testing. This work goes beyond that by using battery pack data from real-world vehicle operation. Our data source is a fleet of 550 battery electric vehicles (BEVs). We aim to provide different feature sets that are accessible to the user groups of the SOH forecasting model like private BEV owners, BEV fleet managers, and battery designers. To this end, we investigate histogram-based features and accessible features. Our results show that a state-of-the-art SOH forecasting method based on histogram features works not only on battery cell data from laboratory operation, but also on battery system data from real-world BEV fleet operation. The model was able to learn the dependence of the SOH from the battery load, i.e., BEV usage. Switching from accessible features to the histogram-based features showed an improvement in model performance of up to 6.1 %. Two use cases for different operating strategies exemplary illustrate how the SOH forecasting model can be applied.

Keywords: Battery aging; forecasting; state of health; lithium-ion battery; battery electric vehicles; machine learning

1 Introduction

Lithium-ion batteries are a well-established power source in mobile consumer devices like notebooks and smartphones [1]. In recent years, however, they have found more and more application in the mobility sector, especially in battery electric vehicles (BEVs). In this application, the battery is estimated to be the most valuable component in 2030, still accounting for 25 % of the total cost [2,3], while it accounts for only 1 % to 4 % of the total cost in smartphones [4,5]. Apart from the cost aspect, BEVs have also higher performance and safety requirements for their high-voltage (HV) lithium-ion battery. In addition, BEVs are experiencing increased demand, which raises interest and the need to address the central component, the battery, in research and industry [2,6–8]. In particular, a deeper understanding of the state of health (SOH) of lithium-ion batteries is of interest as it relates to the ability to meet the performance requirements of the application and the residual value (RV) of the battery. The SOH compares the current state of the battery with the state of the battery at the beginning of life (BOL). As the SOH reflects the battery's aging it highly depends on the usage and environmental conditions of the battery [9–11]. Thus, the future SOH is dependent on the BEV's future usage and environmental conditions.

The assessment of the current SOH with the battery data available at the current point in time is called SOH estimation. When the battery ages, the SOH decreases. Modeling this change of the SOH from a current SOH to a future SOH due to aging causes is called SOH forecasting. These aging causes are encoded in the battery operational load through parameters like state of charge (SOC), temperature, and current [12]. For these tasks the terms SOH estimation, prediction, and forecasting are used ambiguously in the literature. Especially, the terms prediction and forecasting are often used synonymously. However, [13] describe forecasting as prediction about the future so that forecasting seems the more precise term for the task considered in this paper. A further differentiation is discussed in our previous work [12] (see Section 2.1.1 there).

Knowledge about the future SOH is relevant for different user groups in different contexts: For example, private BEV owners, BEV fleet managers, and BEV manufacturers are interested in the battery's future RV, 2nd life applications, vehicle replacement planning, improvements of the BEV operational strategy regarding the SOH, and the battery warranty [12,14,15]. Until now only few forecasting methods exist that are applicable in real-world vehicle operation [12]. For an overview of methods for SOH forecasting like [16,17] we refer to the structured literature review in our previous work [12].

Of all the summarized methods in [12], none use a data set HV lithium-ion battery packs in BEVs operated in real-world vehicle operation (see Appendix Table 12). Moreover, most of these methods use data from lithium-ion battery cells (LIBs) operated in a laboratory (80%) confirming the summary of [18]. Other data sets listed in the Appendix in Table 12, either consist of few electric vehicles (EVs), only plug-in hybrid vehicles (PHEVs), but not BEVs, low-voltage (LV) batteries, or are from non-automotive contexts.

In summary, the data-related major limitations of the existing works are as follows: First, batteries aging in the laboratory show several differences regarding battery operation compared to real-world BEV operation (L1) as listed by [12] and further detailed in this paper in Table 3. Second, most of the batteries operated in laboratory are cells, but not modules or packs which are installed in BEVs (L2). Although the SOH of battery cells, modules, and packs are interdependent, the SOH forecasting methods have not yet been applied to lithium-ion battery pack data from BEVs [12,18–20]. We discuss these limitations in more detail in Section 2. Data sets overcoming these limitations are more expensive and difficult to obtain compared to data from operation of cells in a laboratory: First, battery packs are more expensive than cells. Second, laboratory operation of batteries is usually more intensive to accelerate aging, e.g., by applying higher currents, higher temperatures, or no operational rest periods. As a result, batteries from BEVs require a longer period of operation to undergo significant aging. Third, because of the higher variability of BEV operation more batteries are required to obtain sufficient sampling

points. To overcome the above limitations, data from two domains appear to be appropriate and available: BEVs of private owners or BEVs in Mobility on Demand (MOD) use cases.[1]

To investigate whether the two data-related limitations mentioned above can be overcome, we build our method on our previous work [23] because of its advantages as shown in our structured literature review [12]: It is suitable to encode the variability of battery operational data from BEVs, especially the variable current signal which is non-identical over several cycles as further analyzed in Section 2.2. Also, it can easily be adapted to different forecast horizons by choosing the size of the sliding window. Furthermore, it is transferable to new battery types [24]. We adapt this state-of-the-art method so that features can be examined that are more accessible to different user groups as described in Section 2.3.

The main contribution of this work is to investigate how a state-of-the-art method for SOH forecasting [23] of LIB cells in laboratory operation is suitable to forecast the SOH of a LIB system in vehicle operation (Cell & Lab $\rightarrow$ System & BEV). Therefore, in contrast to existing work on SOH forecasting, we use data from battery operation in a real-world MOD BEV fleet, not from laboratory operation. Further, we contribute an assessment of different feature sets for different user groups of SOH forecasting models. Lastly, the SOH forecasting model is practically applied to forecast the SOH of the BEV fleet under different operational scenarios.

The remainder of this paper is structured as follows: First, lithium-ion batteries, the two mentioned limitations of current data sets, as well as the uncertainty in SOH forecasting are introduced more detailed in Section 2. Afterwards, in Section 3, the state-of-the-art method for SOH forecasting is explained including the newly used features. The used data basis from the MOD BEV fleet operation is presented in Section 4. Subsequently, we present and discuss our results in Section 5. Section 6 concludes our work.

2 State of the Art

2.1 Lithium-Ion Batteries

2.1.1 Battery Cell and Aging

The major components of a LIB are: A negative electrode (anode), a positive electrode (cathode), the ion-conducting electrolyte, and the electrically insulating separator. For a schematic representation of a typical LIB and information on the operating principle, interested readers are referred to [1,25–27]. Regarding the aging characteristics, the cathode material is of high importance [28]. The traditional cathode material has been lithium cobalt oxide (LCO). Alternatives are lithium nickel manganese cobalt oxide (NMC) and lithium iron phosphate (LFP) which have advantages over LCO regarding safety, cost, and size [27].

Battery aging is usually measured by the degradation of the SOH.[2] The SOH can be described by the internal resistance (SOH_R), the capacity (SOH_C), and the energy (SOH_E) [12,29,30]. SOH_R is the relative change of the internal ohmic resistance compared to a new battery. SOH_C denotes the capacity $C(t)$ relative to the called nominal capacity C_{nom} which is specified by the battery manufacturer [31]. Analogous, SOH_E is the total energy $E_{max}(t)$ relative to the nominal total energy E_{nom} [32]:

$$SOH(t) = SOH_E(t) = \frac{E_{max}(t)}{E_{nom}} \tag{1}$$

As [32] state, SOH_C and SOH_E are related via the voltage U because it holds that the energy of a battery is the product of the capacity $C(t)$ and average discharge voltage $\overline{U_{disch}}$ [1]:

$$E_{max}(t) = C(t) \cdot \overline{U_{disch}} \tag{2}$$

Alongside the capacity-based SOH_C, the SOC is commonly known. Analogously to SOH_C and SOC, the energy-based SOH_E has a corresponding state of energy (SOE) defined as [33,34]:

---

[1] For a differentiation of Mobility on Demand (MOD) and Mobility-as-a-Service (MaaS) consult [21,22].
[2] For a detailed introduction to the SOH consider Section 2.1 in our previous work [12].

3

$$SOE(t) = \frac{E(t)}{E_{\max}(t)} \qquad (3)$$

with $E(t)$ as currently stored battery energy and $[E] = Wh$.

The SOH_C and SOC neglect the energy losses of electrochemical reactions and internal resistances inside the battery because they only focus on the charge flow. However, the energy losses may affect the available energy provided to the BEV. Thus, the SOH_E and SOE are more meaningful and practically relevant for the operation of BEVs [33,35]. This is also manifested by BEV manufacturers' common specification of the battery energy content in kWh and not of the capacity in Ah. Likewise, it corresponds to the legal requirement to specify the energy consumption in kWh/100 km for BEV advertisements in Germany [36]. Compared to the SOE, the SOC is useful for batteries with flat and short discharge voltage transients like lead-acid and alkaline nickel batteries. But the steeper and longer discharge voltage transients of lithium-ion batteries are only considered in the SOE, not the SOC, e.g., by the average discharge voltage $\overline{U_{\mathrm{disch}}}$ in Eq. (2) [34,37]. Also, the new United Nations (UN) Global Technical Regulation (GTR) No. 22 will accelerate the importance of the usable battery energy (UBE) and not the capacity as a measure of state because of the UBE's importance for users, vendors, and buyers of BEVs [38,39]. Here, usable energy refers to the available net energy considering possible limitations of the usable SOC range by the BMS in contrast to the total or gross energy [40,41]. For the reasons mentioned above, we focus on the SOH_E, for simplicity referred to as SOH in this work.

Battery aging can be classified into calendar aging and cyclic aging. Calendar aging is associated with the storage of batteries, meaning no charging or discharging is applied. Hence, it is also called passive aging. Cyclic aging corresponds to the impact of battery usage on the SOH, i.e., aging due to charging and discharging [42].

High temperatures (T) and high SOC are causing accelerated battery calendar aging [43,44]. For example, a high SOC over 80% accelerates solid electrolyte interphase (SEI) growth [45]. Other stressors accelerating battery aging are high charge and discharge C-rates[3] as well as a high ΔSOC [42,46]. Even though battery stressors are qualitatively known as displayed in Table 1, their joint impact on the battery's SOH has not been modeled quantitatively yet.

Table 1: Aging mechanisms and their accelerating stressors [47,48]

Battery component	Aging Mechanisms	Accelerated by
Anode	Lithium plating	↑ C-rate, ↓ T, ↑ SOC
	Electrolyte decomposition	↑ T, ↑ SOC
	SEI formation	↑ & ↓ SOC
	SEI decomposition	↑ C-rate, ↓ T
	SEI growth	↑ T, ↑ SOC
	Structural disordering	↑ C-rate, ↑ & ↓ SOC
	Corrosion and loss of electrical contact	↓ SOC
Separator	Blocked pores (Separator and Electrodes)	↑ T, ↑ SOC
Cathode	Dissolving of transition metals	↑ T,
	Binder decomposition	↑ T, ↑ SOC
	Structural disordering	↑ C-rate, ↑ T
	Corrosion and loss of electrical contact	↑ C-rate, ↑ T, ↑ SOC

There exist three main characteristic battery aging trajectories: Linear, superlinear, and sublinear degradation as schematically illustrated in Figure 1. Linear degradation is characterized by a constant aging rate over the whole battery life. In contrast, batteries with superlinear degradation first age slowly, but change to accelerated aging after the knee-point. Sublinear degradation is often associated with SEI growth, which is self-passivating and, thus, self-limiting [49,50].

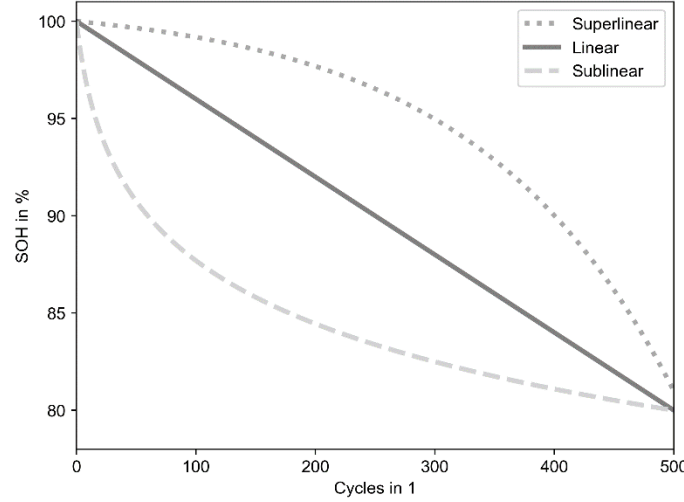[3] C-rate in $1/h = A/Ah$ is the current relative to the nominal capacity C_{nom}.

Figure 1: Schematic types of battery aging trajectories (based on [49])

2.1.2 From Battery Cell to Battery Pack

Most literature focuses on the SOH of battery cells [51–53]. Only few literature focuses on "full battery level", i.e., pack-level [54]. For example, in our literature review [12] only 20 % of the data sets are on pack-level as pointed out in Section 1 (for details see Table 12, Appendix). However, in many applications including BEVs, not single battery cells, but battery packs are used.

A battery pack is an energy storage device composed of one or several electrically connected cells or modules [55,56]. Composing a battery pack of cells, i.e., omitting module assembly, is also called cell-to-pack (CTP) and can reduce parts and increase pack volume utilization [57]. Following ISO/IEC 62620:2014 [55], a battery pack optionally has a package housing as well as a protection unit for control and monitoring. The protection unit for control and monitoring is usually called battery management system (BMS). In contrast to that, Kwade et al. [58] and Kampker [59] require the package housing, the BMS and additionally a cooling system. Väyrynen et al. [56] do not mention these three components at all. Instead, they introduce the term battery system that includes one or multiple battery packs including a cooling system, the BMS and peripherals. The terms battery pack and battery system often appear to be used as synonyms [60,61]. An overview of the discussed definitions is given in the Appendix in Table 13. In our perception, the term battery pack emphasizes that the battery is physically packed somehow. The term battery system emphasizes that the battery is a system composed of several components. In this work, we use the term battery pack following the definition of [55,56]. Extending the battery pack by housing, BMS, and cooling system, we define the term battery system.

The BMS fulfills the following tasks [55,61,62]: Data acquisition, battery state determination, electrical management, safety management, thermal management, and communication. The basis for the other tasks is laid by acquiring data about the cell voltages $V_{cell,i}$, pack voltage V_{pack}, the pack current I_{pack}, and several temperatures at different spots inside the battery pack $T_{pack,i}$. The battery states determined usually are the SOC and SOH. The electrical management controls the charge and discharge process. This includes equalization charging, i.e., cell balancing which ensures that the cells in a pack have the same SOC, i.e., voltage. Cell balancing maximizes the battery's useable amount of charge because the cell with the lowest voltage determines the end of discharging and the cell with the highest voltage determines the end of charging, both when hitting the respective voltage limits. Active cell balancing is only necessary in series connections. Due to Kirchhoff's voltage law cells in parallel connection balance each other automatically [9]. The safety management protects the battery against critical operation like overcharging, overdischarging, high and low temperatures, as well as short circuiting. The thermal management is cooling the battery and equalizing the temperature between cells. In EVs, the BMS is communicating with other devices via the Controller Area Network (CAN) Bus.

A battery module is a group of battery cells in series (s) and/or parallel (p) connection [55,56,58,59,61] as depicted in Figure 2 a) and b). Usually, series and parallel circuits are combined: A parallel

connection consisting of cells in series connection is called parallel-series (ps) connection as in Figure 2 c). A series connection consisting of cells in parallel connection is called series-parallel (sp) connection as in Figure 2 d). For example, 3s4p abbreviates three cells in series and four in parallel. The amount, connection, and split of the cells into modules and packs depends on the battery application. For further information consider [9,59].
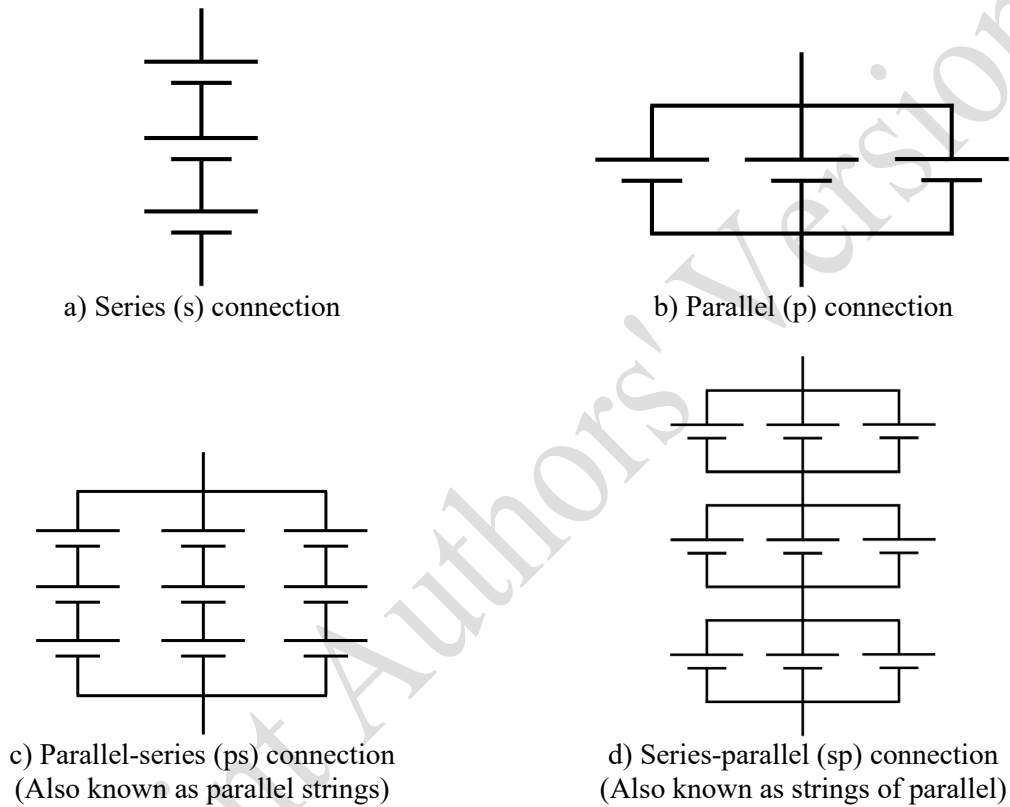

a) Series (s) connection

b) Parallel (p) connection

c) Parallel-series (ps) connection
(Also known as parallel strings)

d) Series-parallel (sp) connection
(Also known as strings of parallel)

Figure 2: Cells in series (s), parallel (p), parallel-series (ps) and series-parallel (sp) connection [19,63–66].[4]

As derived by [12], the SOH of cells in series connection $SOH_{C,s}(t)$ is the cells' minimal $SOH_{C,i}(t)$ assuming C_{nom} is the same for all cells [19,63,70]:[5]

$$SOH_{C,s}(t) = \min_i SOH_{C,i}(t) \text{ with } i = 1,2,\ldots,n_s.$$

(4)

The SOH of cells in parallel connection $SOH_{C,p}(t)$ is the average of all single cells' $SOH_{C,j}(t)$ assuming C_{nom} is the same for all cells [19]:

$$SOH_{C,p}(t) = \frac{1}{n_p}\sum_{j=1}^{n_p} SOH_{C,j}(t) \text{ with } j = 1,2,\ldots,n_p.$$

(5)

---

[4] Feng et al. [67] denote the combined connection topologies vice versa: Our depicted ps connection is denoted as sp connection by them and the sp vice versa as ps correspondingly. They describe their sp as series-connections in parallel and ps as parallel-connections in series. [64] call ps "parallel strings of cells" and sp "strings of parallel cells" but the acronyms are the same. [68,69] use the terminology "parallel cell module" (PCM) for cells within a module wired in parallel and the modules wired in series (here sp). Correspondingly, a "series cell module" (SCM) contains cells wired in series and the modules wired in parallel (here ps).

[5] The assumption that C_{nom} is the same for all cells is not made by Juhlin [19] but mathematically necessary. Its fulfillment is given in practice as the same battery cell type is usually built within one battery module or pack.

Thus, a higher degradation of a single cell has a bigger influence on the SOH in a series connection than in a parallel connection.

Aging of battery modules and systems is more complex than of a single cell because of the interactions of all cells. These interactions cause the degradation process of the battery pack and of the cells in that pack to depend on each other [71]. It is influenced by inconsistencies of cell characteristics, also known as intrinsic cell-to-cell variability [72], electrical imbalance, and temperature gradients between cells that cause heat transfer to adjacent cells [51,73]. For example, Bruen and Marco [74] observe significant differences of cells in parallel regarding their current which results in different temperature distributions and aging of the cells. Jung et al. [75] found that the internal temperature within battery modules is higher than of a single cell because of the heat transfer to adjacent cells. This is especially the case when a single cell is degrading more and its internal resistance increases resulting in higher heat generation [76]. However, cells in parallel strings with initially different SOH_C and SOH_R showed a convergence of the difference [77]. Overall, Dubarry and Beck [78] conclude that effort has been little to study the different inhomogeneities and cell-to-cell variations in battery packs. For more information regarding inconsistency of packs consider [79].

The main drivers of battery aging are the three signals I, T, and SOC. The interdependencies of these signals when switching from cell to pack level are compared in Table 2.

Table 2: Interdependencies of I, T, and SOC on battery aging when switching from cell to pack level.

Signal	Cell level	Module and pack level
I	$I = I_{\text{cell},i}$	I_{pack} splits up to $I_{\text{cell},i}$ depending on series/parallel configuration and $R_{\text{cell},i}$ according to Kirchhoff's laws
T	Heat dissipation by cell i due to $I_{\text{cell},i}$ and $R_{\text{cell},i}$.[6] and $T_{\text{environment}}$	Heat dissipation by cell i due to $I_{\text{cell},i}$ and $R_{\text{cell},i}$, heat transfer with adjacent cells, heat loss to cooling system,[7] and $T_{\text{environment}}$
SOC	$SOC = SOC_{\text{cell},i}$	SOC_{pack} depends on $SOC_{\text{cell},i}$ by the same logic as $C(t)$ and $SOH(t)$ considering the series/parallel configuration and cell balancing

2.2 From Laboratory to Real-World Vehicle Battery Operation

Differences of battery aging data sets from laboratory and real-world vehicle operation have already been discussed by [12]. However, they present both as sharply distinct from each other. In the following, we show a smooth transition from controlled laboratory to uncontrolled real-world vehicle battery operation characterized by the current profile applied to the battery. Finally, we define further criteria of distinction than the current profile in Table 4. The introduced classification schema, i.e., taxonomy, shall enable a more precise differentiation of battery operation and corresponding data sets in the future.

Battery operation can be differentiated by the current profile applied to the battery as structured by the 2x2 matrix in Table 3. We define the current profile as the abstracted time series signal of the current I or C-rate applied to a battery for charging and discharging. The abstracted time series does not consider any small variation of the current due to current control, e.g., during constant current (CC) and constant voltage (CV) phases. During charging, excluding brake energy recuperation during driving, usually charging protocols are used so that the differences between laboratory and real-world operation usually originate from the discharging operation. Petrovic [80] distinguishes three modes of discharge: CC, constant load, and constant resistance. However, as he notes, automotive applications face variable discharging.

---

[6] In laboratory operation of single cells usually no cooling system, but a heating chamber is used to accelerate aging. We consider convection as possible, but radiation as negligible.

[7] In battery packs, we consider radiation and convection as negligible.

Table 3: Characterization of battery aging data sets in a 2x2 matrix by current profile applied to the battery. The arrows show direction from laboratory to real-world vehicle operation data.

| | | **Current** | |
		Constant Current (CC) steps (optional constant voltage (CV) phase)	**Variable Current (VC)**
Current profile over cycles	**Identical (I)**	I-CC: 1) 1 CC step [81–83] 2) Multistage CC steps (MCC) [84,85]	I-VC: 1) Replay of recorded current profile from vehicle [86,87] 2) Representative profile [86,88–94] 3) Driver following predefined profile [95]
	Non-identical (NI)	NI-CC: 1) CC steps with randomized current [96,97]	NI-VC: 1) Real-world vehicle operation [98–100]

From laboratory to real-world vehicle battery operation

We propose two criteria to differentiate battery aging data sets: First, we distinguish whether the current profile is identical (I) over all cycles, usually for laboratory operation, or non-identical (NI) over all cycles (Rows of Table 3). Second, we distinguish whether the profile has a CC or variable current (VC) in the columns of Table 3.[8] When having CC, also optional short CV phases are included, i.e., non-CC shall not be caused by a controller during a VC phase.

Thus, with CC steps and optional CV phases, we obtain the 1st type of I-CC with an identical, single CC step and an optional CV step (I-CC.1) and the 2nd type of I-CC with identical, multistage CC (MCC) steps (I-CC.2). These two are common types of charging protocols [102]. The exact time length of the CC steps may vary due to battery aging.

The next step towards real-world vehicle battery operation is still with CC steps, but the CC steps of different cycles are non-identical (NI-CC). This may be the case if the current of each CC step is randomly sampled such as in [96]. The random CC sampling better represents practical battery usage than non-random CC operation [103].

Further, with VC the current profiles of different cycles can be still identical (I-VC), as, first, the current profile can simply be a replay of a recorded profile, e.g., from vehicle operation that is repeated for each cycle (I-VC.1). Second, the current profile can be defined by a representative profile (I-VC.2). Examples are the Worldwide Harmonised Light-Duty Vehicles Test Procedure (WLTP)[9] [104], Urban Dynamometer Driving Schedule (UDDS) [105] or any representative driving cycle (RDC) that aggregately represents real-world operation [106]. Third, a unique professional driver can reproduce a certain current profile on a private track as in [95] (I-VC.3). In this case, the current profiles can only approximately be identical over several cycles.

---

[8] These criteria are also called "change during a single cycle" (CC vs. VC) and "change between different cycles" (I vs. NI) by [101].

[9] The older New European Driving Cycle (NEDC) (German "Neuen Europäischen Fahrzyklus" (NEFZ)) consists of linear slopes and phases of constant velocity. During the phases of constant velocity the current profile will be constant as well.

Lastly, non-identical current profile over several cycles and VC (NI-VC) specifies real-world vehicle operation in which no cycle-wise exact current patterns can be found. This is caused by different drivers, routes, traffic, weather, etc.

Summarized, there is a transition of battery aging data sets from strong laboratory conditions to real-world vehicle operation from I-CC via NI-CC, I-VC to NI-VC. Further criteria of distinction are mentioned in Table 4: First, the place of battery operation will likely be a test bench for I-CC, NI-CC and I-VC except I-VC.3 or alternatively a vehicle for I-VC.3 and NI-VC. Second, most data sets from test benches either have cyclic or calendar aging. Data sets applying cyclic and calendar aging to the batteries are rare [83]. However, in real-world vehicle operation, this is normal with dominating calendar aging [12]. Third, also for real-world vehicle operation, normally batteries in vehicles have a cooling system. This is usually not the case for operation on a test bench. Fourth, the battery environment temperature on test benches is usually either a nearly constant room temperature or defined by a heating chamber. In real-world vehicle operation, the batteries face the outdoor temperature with seasonal changes. Fifth, most battery aging data sets use single cells. Battery modules are rarely used on test benches and only in small quantities as in [107] (I-CC.1)[10] and [108] (I-VC.1).[11] Battery packs are built in vehicles I-VC.3 and NI-VC, but when such data sets are used, e.g., by [98,99], they have not been published, probably due to confidentially.

Table 4: Further criteria to distinguish battery aging data sets.

Criterion	Possible Value
Place of battery operation	Test bench or in-vehicle operation
Aging categories	Cyclic or calendar aging
Cooling system	Yes or no
Environment temperature	Room temperature, Heating chamber, or outdoor temperature with seasonal changes
Battery type	Cell, module, or pack

2.3 Uncertainty in State of Health Forecasting

Forecasting makes statements about the future that is flawed by uncertainty. This uncertainty for SOH forecasting is about the future battery, BEV, or BEV fleet usage. He et al. [109] and Saxena et al. [110] describe this as operational environment uncertainty. We address the uncertainty about the future battery usage by using scenarios to understand the implications of battery usage on battery aging. In doing so, we characterize each scenario by assumptions about the future that are expressed in the model inputs. Scenarios are already common in strategic decision making under uncertainty [111–113]. Porter [113] defines a scenario as "an internally consistent view of what the future might turn out to be." Thus, it is not a forecast, but only a likely reality of the future. As Porter [113] notes the assumptions characterizing a scenario might affect and violate each other. The latter can lead to the elimination of scenarios.

Parallel to Porter's [113] definition, we define usage scenarios of a machine like a BEV as a consistent view of the future usage of the machine. The definition can also be applied to fleets of machines following a definition of the term fleet [114]. Each usage scenario is based on plausible assumptions about important uncertainties regarding the machine's future usage. Building on a single scenario, a set of usage scenarios should reflect a range of possible future usages with important implications for machine aging. Ensuring consistency of assumption about the future usage within a scenario can be difficult. Especially physical consistency may be difficult to assess, e.g., the range of a BEV is reduced due to the future load, but the assumption of range reduction may be inaccurate, affecting usage and ultimately aging.

As in strategic decision making under uncertainty also in our work, the outcome of scenarios may range from trend to extreme scenarios. Trend scenarios assume the same usage in the future as in the past

---

[10] [107] only provide data of 4 packs each with 11 NMC 40Ah cells (4s11p) operated in series connection.
[11] [108] only provide data of 2 packs each with 16 cells (16s1p) operated for 20 and 200 cycles respectively.

(ceteris paribus) or only small changes. Positive and negative extreme scenario correspond to the best and worst case respectively. Apart from the outcome of a scenario an estimated probability can also express the likelihood of the scenario, i.e., the prediction interval [115].

Such scenarios can be based on concrete users or generalized personas regarding the BEV usage. Personas give a face to the user by specifying a fictional but still concrete representation of a target user and are a common tool in product development [116,117]. E.g., a persona may be characterized regarding her BEV usage, e.g., by mainly AC- or DC charging, mainly short-distance or long-distance trips either on rural roads or on highways. Also a persona describing a family with short-distance trips during the week, but long-distance trips at the weekend to visit friends and relatives is possible.

From our point of view, the time period of the usage scenarios should cover a time horizon in which measurable and relevant aging of the machine can happen. This makes the scenarios distinguishable regarding different aging for the model users. For most machines and also for vehicles, this therefore rules out scenarios with a length of seconds or minutes. From our perspective, scenarios need to span weeks, months, or years.

In the Section 1, the users of SOH forecasting models were distinguished as private BEV owners, BEV fleet managers, and battery designers. Each of these users of the model needs to express their assumptions about the future usage of the battery, i.e., the BEV, in the inputs of the SOH forecasting model. Given their different levels of technical experience and knowledge, we want to provide suitable model inputs for each user group. We assume that choosing simpler, but more interpretable and accessible model inputs, i.e., features, like the mileage may reduce the model's performance, but increase usability for users with little technical knowledge. For example, drivers may have a gut feeling for the distance of 1,000 km, but little experience in translating that into a number of required fast charging sessions. Also, the translation from driving in eco vs. sport mode into technical changes, e.g., of the maximum discharge current is unknown and unimportant to most drivers, but relevant to battery designers.

3 Method

We build our method upon the state-of-the-art work of [23] which is shortly introduced in Section 3.1. An overview of methods for SOH forecasting is given in a structured literature review in our previous work [12]. There, we differentiate SOH estimation, i.e., the determination of a state, from SOH forecasting, i.e., the determination of a state change among others by two criteria: First, the relative temporal position of the model inputs and, second, what the input features of the model encode. For SOH estimation, the features encode the effect of the battery aging, like the SOH or capacity trajectory (autoregressive models), or changes in the partial charging curves. These data are obtained from the past or present until the current point in time t_1. Examples of such methods are presented by [118] and the reviews [45,119–121]. For SOH forecasting, the features encode the causes of the battery aging, i.e., the battery operational load. The data on causes of battery aging is obtained from the current point in time t_1 until the end of the forecast horizon t_2. This is required for training, while for interference, i.e., prediction, scenario-based adaptions can be made expressing the future battery operational load, e.g., halving the amount of high-power charging (HPC) events.

In Section 3.2, we present features to encode battery operation, in particular accessible features as alternative to histograms from the state-of-the-art work of [23].

3.1 State of Health Forecasting

For this work, we chose to apply the base method from state-of-the-art work [23] depicted in Figure 3 for several reasons: First, it fulfills the five key criteria examined in our structured literature review [12]. Second, the histogram features presented are suitable to encode the variability of real-world operation, especially the variable current signal which is non-identical over several cycles (VC-NI) as analyzed in Section 2.2. Third, the window-based method allows easy adaption to other features for different user groups as argued in Section 3.2.

As mentioned in Section 2.1, battery aging is perceived as a state change from a current $SOH(t_1)$ to a future $SOH(t_2)$ due to aging causes. The aging causes are encoded in the battery operational data which consist of multidimensional time series signals of C-rate, temperature, and SOE. As depicted in Figure 3, first, this battery operational data from the window $[t_1, t_2]$ is used to extract stressor data of battery stressor types which are known to induce battery aging. Types of stressor data applied in this work are introduced in Section 3.2. Second, the stressor data is input of a machine learning (ML) model, that outputs the state change ΔSOH from a current $SOH(t_1)$ to a future $SOH(t_2)$. As the training is supervised, both SOH values need to be known in the training phase. Nevertheless, in a production phase, only the $SOH(t_1)$ needs to be known.
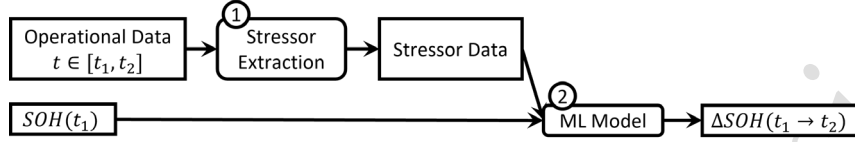

Figure 3: Model structure - stressor extraction (1) and ML model (2) [23]

The window $[t_1, t_2]$ is favorable either over the equivalent full cycle (EFC) or over the time as battery aging can be cyclic or calendar aging. For better comparability with other methods, which are normally based on the EFC, a sliding window approach based on the EFC is chosen to derive training samples as in state-of-the-art work [23]. A window is specified by the cycle window width (WW) w_w which defines the number of EFC between the current $SOH(t_1)$ and future $SOH(t_2)$. The cycle WW defines for how many future cycles the model learns to forecast the SOH (forecast horizon). The input length, i.e., the number of features is independent of the window width. To extract further training samples the cycle window is shifted by the window shift (WS) w_s.

Thus, the WS controls the number of generated samples and the amount of new operational data in each sample as the window shifts forward through time. If the WS is larger than the WW, some sections in the degradation curve would be skipped, leading to a loss of information. Thus, this case is not considered. More advantageous are the following two: If the WS equals the WW, each sample contains entirely new operational data. If the WS is smaller than the WW, the windows are partially overlapping.

The desired accuracy of the SOH forecast will likely depend on the application of the SOH forecasting model: Is the forecast for new or old batteries? Is a rough forecast of those batteries close to EOL desired or a precise result for recommendations regarding the battery operational strategy? Based on the assumption that the relevant SOH range is from 100 % to 80 % in the automotive sector an error of +/- 1 % SOH for SOH forecasting seems just acceptable compared to an error of +/- 0.1 % SOH which might be acceptable.

3.2 Stressor Data
In this work, we extract two types of stressor data in step one in Figure 3 that are input of the ML model. Further stressor data without motivation from the literature is out of scope in this work. We use histograms as in state-of-the-art work [23] but also other stressors more accessible for non-domain experts, inspired by other existing works on SOH forecasting, are motivated. Thus, by using different stressor data features we examine the trade-off between model performance and feature interpretability for the model's user. Therefore, we keep the same time windows, i.e., the same $SOH(t_1)$ as features and the same ΔSOH as output variables. This maintains the output value distribution and, thus, improves comparability among the different stressor data.

Histograms

Histograms[12] of different dimensionalities (1D, 2D, 3D) based on C-rate, temperature, and SOE have been used as stressor data [23]. Therefore, the signal interval width is defining the sampling granularity of the signals' bins. E.g., the temperature signal could be split into intervals of 1 °C or 2 °C. The signal

---

[12] These histograms are called load spectrum or load collective in the field of mechanical fatigue analysis of machines and materials [122].

interval width also influences the number of features, i.e., the input length. The suitability of multi-dimensional residence time histograms has already been shown for SOH forecasting with LIB cell data from laboratory operation [23] and also regarding transferability among different cell data sets [24].

Accessible Features

The more accessible features described in Table 5 are either inspired by other papers on SOH forecasting or motivated by possible user groups of SOH forecasting models. They either reflect cyclic or calendar aging.

The term "accessibility" here refers to features that are easy to use and understand by the user groups. For example, users with little BEV experience can interpret 1,000 km of driving as with an internal combustion engine (ICE). They may also have a gut feeling for the usual number of their AC- and DC-charging events per week why we choose this as an accessible feature. Also, as values based on experience for low or high fuel consumption exists, such experience for the energy consumption, e.g., in kWh/ 100 km may develop. From there an estimate of a energy throughput E_{thrpt} required for a certain distance and terrain can be derived.

Private BEV users may choose a certain driving mode to adapt the vehicle's performance, e.g., regarding regenerative braking strength, or decreasing the accelerator pedal responsiveness for quick acceleration [123]. Further, an ECO mode could restrict the maximum power output to 80%, i.e., the maximum discharge current $I_{\text{dr,max}}$ assuming CV. The maximum available discharge current is easily adaptable and a method to slow down battery aging.

For the operation and management of BEV fleets different viewpoints are relevant [114,124]: A role like a shift or operation manager might consider in the short term the amount of available BEVs and their SOE at shift beginning ($SOE_{\text{park,mean}}$). Further, a head of operations might be responsible for vehicle replacements by a new vehicle generation. Both shall not be required to acquire deep technical understanding, just as a private BEV user. However, they may be supported by a vehicle data analyst who has the technical understanding.

Table 5: Overview of accessible features

	Name	Symbol	Unit	Reference
Cyclic aging	Cycles from t_1 until t_2	k	EFC	[100,125–127]
	Delta mileage	Δd	km	[128,129]
	Number of AC charging processes	n_{AC}	-	[130]
	Number of DC charging processes	n_{DC}	-	[130]
	AC charging energy throughput	$E_{\text{thrpt,AC}}$	Wh	
	DC charging energy throughput	$E_{\text{thrpt,DC}}$	Wh	
	Absolute max. charging current	$I_{\text{ch,max}}$	1/h	[128,131,132][13]
	Mean charging current	$I_{\text{ch,mean}}$	1/h	[128,131,132][13]
	Standard deviation (SD) of charging current	$I_{\text{ch,SD}}$	1/h	[128,131,132][13]
	Absolute max. current while driving [14]	$I_{\text{dr,max}}$	1/h	[128,131,132][13]
	Mean current while driving	$I_{\text{dr,mean}}$	1/h	[128,131,132][13]
	SD of current while driving	$I_{\text{dr,SD}}$	1/h	[128,131,132][13]
	Min. temperature	T_{min}	°C	[131]
	Max. temperature	T_{max}	°C	[131]
	Max. SOE	SOE_{max}	%	
	SOE lift [15]	ΔSOE	%	
Calendar aging	Parking time	Δt_{park}	h	[89]
	Mean parking SOE	$SOE_{\text{park,mean}}$	%	[89]
	Mean parking temperature	$T_{\text{park,mean}}$	°C	[89]
	Time from t_1 until t_2	Δt_{total}	h	[131]

4 Data basis

Using battery system operational data from real-world BEV operation, i.e., with non-identical current profiles over several cycles and VC (NI-VC) as introduced in Section 2.2, seems to become feasible as the registrations of BEVs have increased worldwide in the past years [7]. But the majority of these BEVs are used privately and are parked most of the time, e.g., approximately 89-97 % in Germany [133–135]. Battery aging is correspondingly slow, so data from BEVs operated in such a way will only be be suitable for creating SOH forecasting models in the future. In contrast to the domain of private BEVs, BEVs in Mobility on Demand (MOD) use cases are operated more intensively and age quicker [12,136]. Therefore, data from the domain of MOD BEV fleets is more suitable nowadays to apply SOH forecasting on real-world BEV operational data.

Thus, we base our work on battery pack data of 550 BEVs operated in a ride-pooling MOD shuttle service in two large German cities. The total time span of data logging is 27 months including a total of 7 months operational pauses due to COVID-19 restrictions. During the total time span the vehicles drove a total of 39.1 million km corresponding to 115,239 EFC. Based on the average total ΔSOH and the total EFC, the mean SOH decline is 0.017 % SOH per EFC. The energy throughput by charging was 53 % AC and 47 % DC with up to 7.2 kW and 100 kW charging power respectively. I.e., the highest charging C-rate of 1.25 is comparatively moderate.

---

[13] [132] use statistical properties of I_{disch}. [131] use I_{mean}. As it remains unclear whether it refers to charging or discharging, we derive $I_{\text{ch,mean}}$ and $I_{\text{dr,mean}}$ when $I \neq 0$. Also, our data set does not include Q_{thrpt} and SOC. Thus, we use the correlating E_{thrpt} and SOE instead respectively. [128] propose distributional information of the C-rate during cycling.

[14] Not a Number (NaN) values are not included. $I_{\text{dr,min}}$ means $min(I_{\text{dr}})$ if drive modus, i.e., including internal charging due to break energy recuperation. Also $I_{\text{dr}} < 0A$ for discharging.

[15] We assume $\Delta SOE = SOE_{\text{max}} - SOE_{\text{min}}$. In their data set André et al. [131] only have ΔSOE of 60% and 100%.

The HV system of the BEV is based on NMC-622 pouch cells. The BEV has a nominal energy content $E_{\mathrm{nom,pack}}$ of 87 kWh and a nominal capacity $C_{\mathrm{nom,pack}}$ of 240 Ah. The BEV enables storing braking energy (braking recuperation) as well as coasting energy (coasting recuperation) of the motors. Via a DC/DC converter, the HV battery system also supplies the 12 V on-board electrical system for air conditioning, USB chargers, etc.

Table 6: Details about used signals.

Signal	Sampling Time in s	Resolution	Calculated offline
Current I	10	$1\,A \triangleq \frac{1A}{240Ah} = 0.0042C$	-
Temperature T	~120	0.5°C	-
SOE	10	0.5 %	-
Energy E	10	50 Wh	-
Mileage	~60	1 km	-
BEV-mode	10	-	-
EFC	10	~0.0025	f(SOE), see. Eq. (6)
SOH	10	~0.36 %, see Eqs. (10)-(18)	f(E, E_{nom}, SOE), see. Eq. (7)

The sampling time and signal resolution of the relevant time series signals are given in Table 6. The BEV-mode is driving (discharging or charging, i.e., recuperation), charging (externally by AC or DC), or parking. The EFC and the SOH are calculated offline as part of the data cleansing:

$$EFC(t) = \left| \frac{\sum_{i=t_0}^{t-1} |SOE(i+1) - SOE(i)|}{200\%} \right| \tag{6}$$

$$SOH(t) = \frac{E_{\max}(t)}{E_{nom}} = \frac{E(t)}{SOE(t)} \cdot \frac{1}{E_{nom}} \tag{7}$$

with applying a symmetric weighted moving average with a manually-tuned time window of 10 d to smooth the SOH signal. This smoothed SOH value over EFC is shown as a boxplot of the whole fleet in Figure 4.

Inference from this plot to the average energy consumption of the fleet is not straight forward because the BEVs have different SOH values at their BOL and the start of data logging. Especially their SOH at BOL may be not 100% because of the definition of E_{nom}. Also, for each BEV a different mileage span is logged during the logged time span. Thus, comparability to other SOH trajectories is not easily possible. At the beginning a sublinear decrease transitions to linear aging. After 400 EFC only few data is available, i.e., fleet SOH values need to be interpreted carefully there.
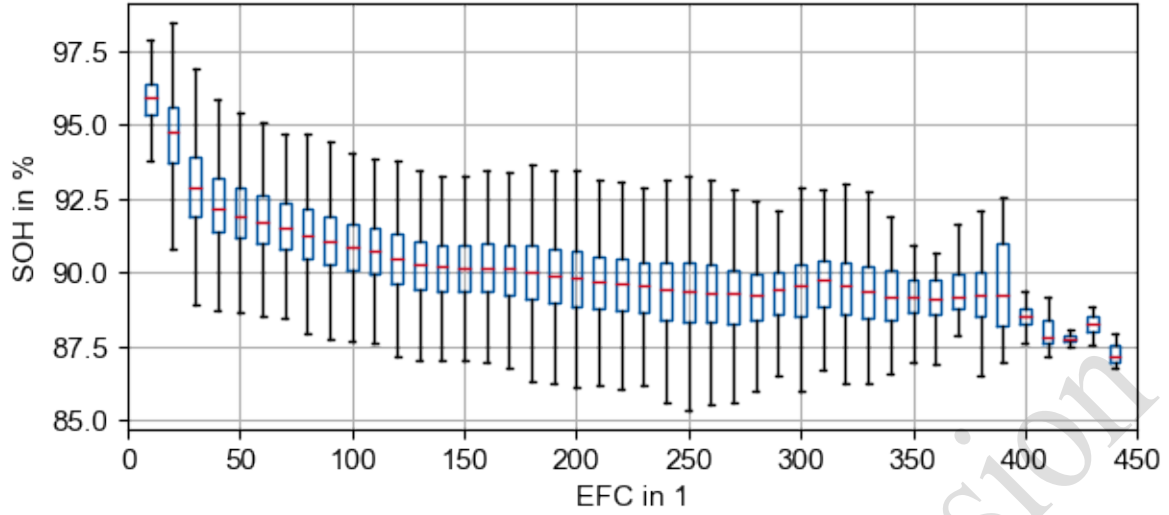
Figure 4: Fleet SOH curve.

Sufficiency of the Sampling Time

When analyzing the sampling times of the signals given in Table 6, it is clearly visible in Figure 5 that a sampling time of 10 s is too high to accurately capture the discharge current signal of real-world vehicle operation. For example, an acceleration phase of a few seconds after a stop at city traffic lights with different characteristic current profiles depending on the driver would not be captured accurately. For CC charging such a higher sampling time is less critical. Also, for SOE and temperature a smaller sampling time is sufficient because they are both less dynamic, i.e., only change slowly in a period of time of about up to 100 s.
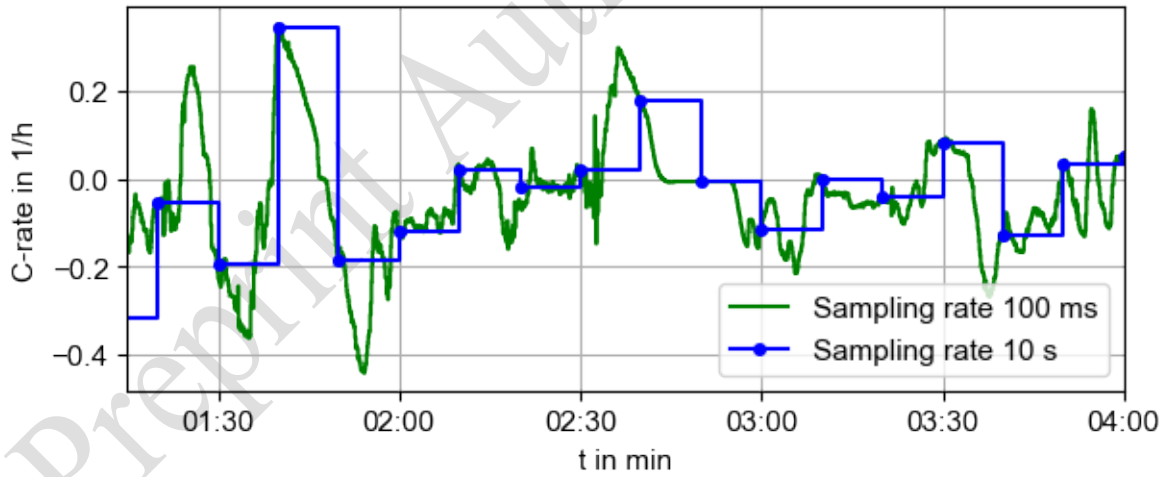

Figure 5: Exemplary comparison of the current signal with different sampling rates.

Greenbank and Howey [137] used histogram-based features for SOH forecasting as well. They concluded that increasing the sampling time of the two applied data sets [84,85] from 1 s to 100 s resulted in no difference of performance [137]. However, the two data sets used CC discharging so only little information was lost by the increased sampling time. This limits the applicability of their finding to our data set.

Considering the histogram-based stressor data proposed in Section 3.2, we are interested in the quality of approximation of the used histograms based on signals with a lower sampling time by a histogram based on signals with a higher sampling time. This applies especially to the discharge current signal. As depicted in Figure 6, approximating discharge current histograms based on 100 ms sampling time

15

with histograms based on a 10 s sampling time seems feasible, even if deviations exist. Notably during driving-mode at C-rates around zero the largest deviation exists. However, those very low C-rates have no substantial effect on battery aging. Still, all deviations mark a limitation of the used data set.
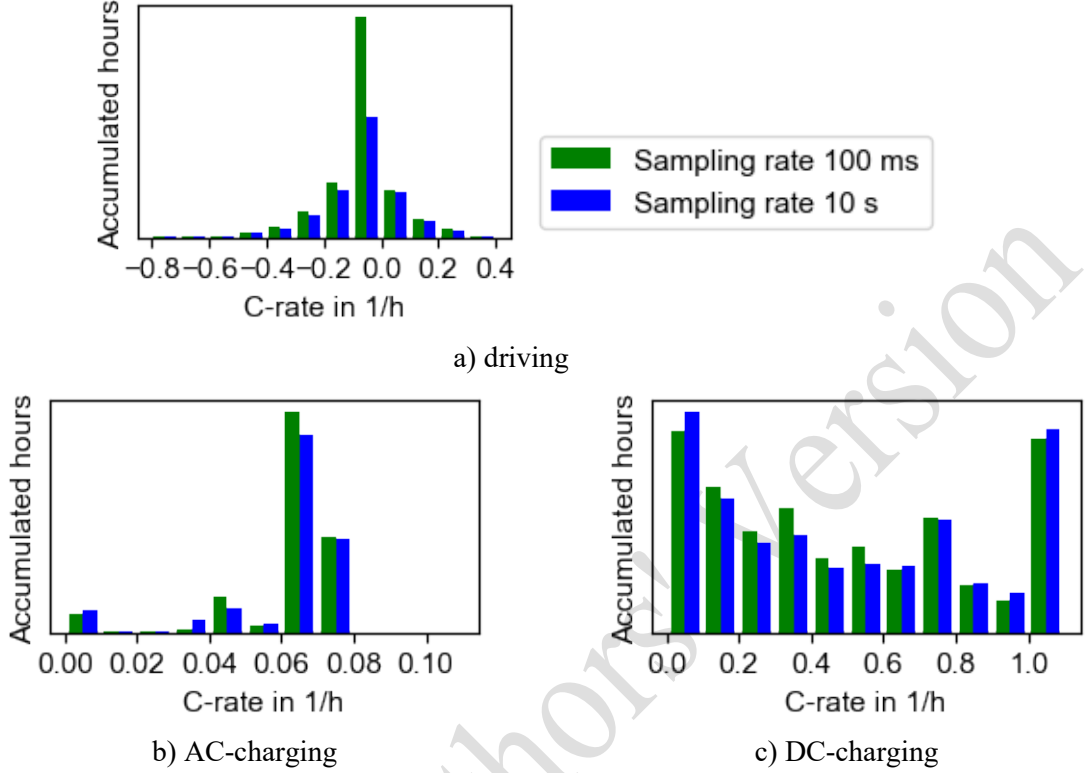

Figure 6: Approximation of histograms with high and low sampling time during a) driving, b) AC-charging, c) DC-charging.

5 Results and Discussion

In Section 5.1, we present the Design of Experiments (DOE) which is followed by the evaluation of the defined experiments in Section 5.2. The two types of stressor data defined in Section 3.2 are first evaluated separately and then compared with each other. Finally in Section 5.3, we apply one SOH forecasting model in two scenarios under changed operational conditions as proposed in Section 2.3.

5.1 Design of Experiments

Analogous to the defined stressor data in Section 3.2, histogram-based features and accessible features, we conduct two series of experiments as presented in Section 5.1.1 and Section 5.1.2 respectively.

We did not apply a feature selection method because we want the complete operational space of I, SOE, and T to be part of the model inputs. Also, as motivated and discussed in [12], we are aiming at a method to derive features that enables transfer learning and, therefore, is valid for multiple data sets. But transfer learning is not possible when different features are selected for different data sets.

5.1.1 Histogram-based Features

For showing the suitability of the chosen SOH forecasting method on a data set from battery systems in BEV fleet operation, it is essential to find good hyperparameter values of the stressor extraction described in Section 3.1. The five hyperparameters are examined in decreasing order of the influence of the parameter on the model performance based on experience from this work and our previous work [23] as shown in Figure 7: First, we examine the WW and WS of the time window as well as the signal interval width for current, temperature, and SOE (Experiment 1-3). Thereby, we aim at finding the right balance of input features and training samples. Further, we examine different combinations of the current, temperature, and SOE signals to stressor tables for charging, discharging, and parking mode (Experiment 4 & 5). We also examine the capability of the SOH forecasting model to generalize.
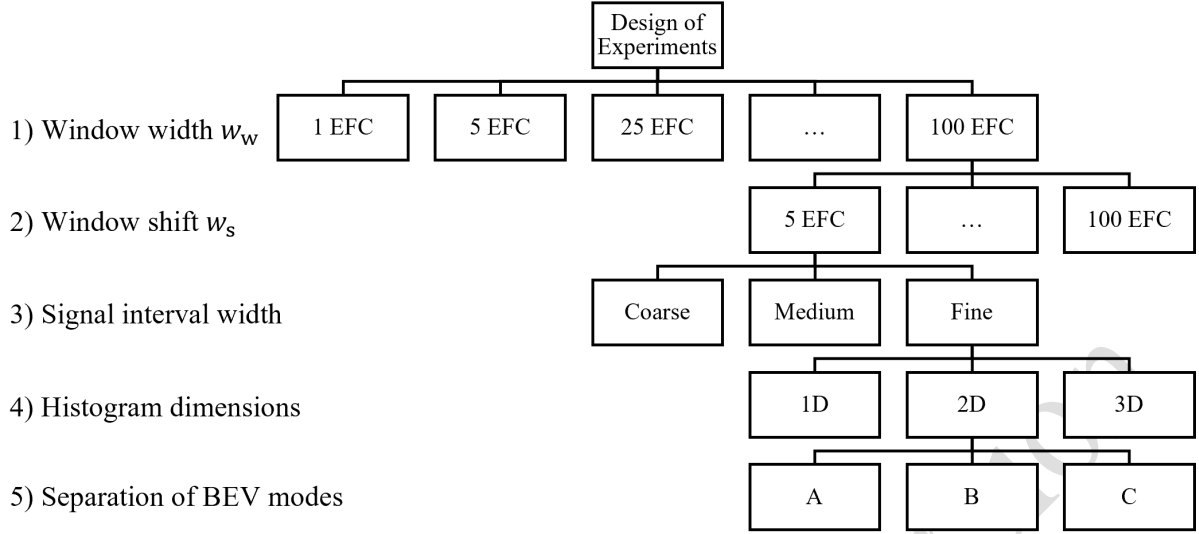
	Design of Experiments				
1) Window width w_w	1 EFC	5 EFC	25 EFC	...	100 EFC
2) Window shift w_s			5 EFC	...	100 EFC
3) Signal interval width		Coarse	Medium	Fine	
4) Histogram dimensions			1D	2D	3D
5) Separation of BEV modes			A	B	C

Figure 7: Structure of Design of Experiments for the histogram-based features.

At the start of the DOE, we set the initial parameters as follows based on experience from this work and our previous work [23]: Window shift $w_\mathrm{s} = 5$ cycles, except if $w_\mathrm{w} = 1$ cycle as $w_\mathrm{s} \leq w_\mathrm{w}$ should be true. We used signal interval width coarse, 2D histograms and BEV mode A for the 2D stressor tables based on our previously published insights [23]. 2D stressor tables, variant A was modified by substituting "discharging" by "driving" which now includes micro-cycling due to regenerative braking.

Experiment 1: Window Width w_w

First, w_w determines the forecast horizon and the number of cycles corresponding to the histograms aggregating the operational data. Thus, it also influences the distribution of the output value ΔSOH which the ML model has to learn. The selection of w_w depends on how many cycles sensibly can be aggregated together to offer sufficient variance among the histograms for the ML model to distinguish the samples. The selection of w_w is inspired by forecast horizons listed in our structured literature review [12] like 30 cycles [138], 40 cycles [139], and 25 to 530 cycles [23], but also 1 cycle [17,127,131,132,140,141]. Furthermore, the relevance of the forecast horizon for BEV users and fleet managers is considered. Given the fleet's SOH trajectory in Figure 4 with up to 450 cycles, larger w_w like in our previous work [23] with data up to around 1000 cycles prohibits generating at least a few samples from each battery system. Thus, we choose $w_\mathrm{w,single} \in \{1, 5, 10, 25, 50, 100\}$ (W1 to W6). We also combine these w_w because this showed improved generalization on battery cell data in our previous work [23]: $w_\mathrm{w,combined} \in \{\{10, 25\}, \{25, 50\}, \{50, 100\}, \{10, 25, 50\}, \{25, 50, 100\}\}$ (W7 to W11).

Experiment 2: Window Shift w_s

Second, w_s influences how many cycles the window is shifted during sample generation, i.e., how many samples are generated. Thus, its setting needs to ensure sufficient sampling points for the ML model to learn from and to acquire the ability of good interpolation in between the sampling points, i.e., a good model fit. We choose w_s depending on w_w because of their interaction as $w_\mathrm{s} \in \{5, 10, 25, 50, 100\}$ cycles with $w_\mathrm{s} \leq w_\mathrm{w}$ to avoid skipping operational data, as mentioned before.

Experiment 3: Signal Interval Width

Third, the signal interval width, i.e., the width of the histograms' bins, determines the amount of features in the histograms. A finer signal interval width enables the histograms to represent the underlying time series data more precisely. We specify fine, medium, and coarse signal interval width (F, M, and C respectively) for current, temperature, and SOE in Table 7. Combining different signal interval widths like different w_w is not possible because they have different input feature shapes requiring different input layers. Compared to our previous work [23], we adapt the granularity of the current and

temperature bins because their overall range is different in this data set. For the C-rate an additional interval for zero current is introduced, representing the parking mode.

Table 7: Signal interval width for current, temperature, and SOE

		Current in 1/h	Temperature in °C	SOE in %
Bin range		[-1.5, 1.5]	[-20, 50]	[0, 100]
Bin width	**Fine (F)**	0.1	3	5
	Medium (M)	0.3	5	10
	Coarse (C)	0.5	10	20

Experiment 4: Histogram Dimension

Forth, the dimension of the histogram can either be 1D, 2D, or 3D, i.e., one, two, or all three signals of T, I, and SOE are combined in one histogram. A lower dimensional histogram can be seen as a column-wise or row-wise aggregation of a higher dimensional histogram. Thus, lower dimensional histograms have fewer features, but lack a representation of the signals' interdependence.

Experiment 5: Separation of BEV Modes

Fifth, histograms depending on the BEV mode are examined as listed in Table 8: Separate histograms for charging, driving & parking (BEV mode A), AC-/DC-charging, driving & parking (BEV mode B), and joint histograms for all BEV modes (BEV mode C) are differentiated. Thus, BEV mode C has only three histograms (T & SOE, I & SOE, I & T) and does not differentiate the BEV mode.

Table 8: Combined signals for 2D stressor tables by BEV mode.

	T & SOE	I & SOE	I & T
BEV mode A [16]	Charging, Driving, Parking	Charging, Driving	Charging, Driving
BEV mode B	AC-Charging, DC-Charging, Driving, Parking	AC-Charging, DC-Charging, Driving	AC-Charging, DC-Charging, Driving
BEV mode C	No differentiation	No differentiation	No differentiation

5.1.2 Accessible Features

We aim at finding a set of accessible features for non-domain experts, i.e., of non-histogram scalars that represent battery load as motivated in Section 3.2. In experiment 1, we only use $SOH(t_1)$, to determine suitable w_s for $w_w = \{10, 25, 50, 100\}$ from experiment 1 with histogram-based features. Then, in experiment 2a and 2b cyclic and calendar aging features are analyzed respectively. Next, all of these features are combined in experiment 3.1 and only the best of experiment 2a and 2b are combined in experiment 3.2. We structure all experiments with accessible features in Table 9.

---

[16] Called variant A in our previous work [23].

Table 9: Other feature sets used as stressor data.

Experiment No.	Start $SOH(t_1)$	Cyclic Aging k	Δ mileage	n_{AC} & n_{DC}	$E_{thrpt,AC}$ & $E_{thrpt,DC}$	$I_{ch,dr}$ [17]	T_{min}, T_{max}	$SOE_{max}, \Delta SOE$	Calendar Aging Δt_{park}	$SOE_{park,mean}$	$T_{park,mean}$	Δt_{total}
1	x											
2a.1	x	x										
2a.2	x		x									
2a.3	x			x								
2a.4	x				x							
2a.5	x					x						
2a.6	x						x					
2a.7	x							x				
2b.1	x								x			
2b.2	x									x		
2b.3	x										x	
2b.4	x											x
3.1	x	x	x	x	x	x	x	x	x	x	x	x
3.2	x				x	x						

5.1.3 General Settings

Each data set generated with a different setting of histogram-based or accessible features as described in Section 5.1.1 or 5.1.2 respectively, was split to enable evaluation of the model's generalization performance. First, to enable evaluation of the model's generalization performance on different vehicles than in the training and validation data set, 5% of the vehicles were chosen as test vehicles (2. Test). I.e., this tells about the model's forecast performance on new vehicles that recently joined the fleet without any time series used for training sample generation. Second, the samples of the remaining vehicles were split into the training, validation, and test data (1. Test) by the ratio of 80:10:10, reaching an overall ratio of 76:9.5:9.5:5 for training, validation, and the two test sets. The training data set was used to fit the model's parameter and the validation data set served for early stopping and hyperparameter optimization. The 1st test data set enables evaluation of the model's generalization performance on the same vehicles as in the training and validation data set. E.g., neighboring time windows may not be in the same data set.

We apply min-max-normalization to each data set based on the minimum and maximum values of the training data set. Similar to our previous work [24], we scale $SOH(t_1)$ separately from the other features. The histograms are also scaled separately for the BEV modes, i.e., AC-/ DC charging, discharging, parking, to preserve the relations within each BEV mode. Otherwise the values of charging and discharging would be very small due to larger parking times. We scale the accessible features separately from each other because they have limited physical relation to each other.

As ML model, we choose a multi-layer perceptron (MLP) because it showed good results in previous work, also in comparison to other ML and deep learning models [23,142]. For each data set a corresponding hyperparameter optimization was executed using Hyperopt version 0.2.7 with Tree-structured Parzen Estimator (TPE) which resulted in a final model for each data set [143,144]. Hyperopt parameters were set to a maximum of 500 evaluations and 100 random startup evaluations. The mean squared error (MSE) on the validation data set was set as optimization metric for the hyperparameter optimization. The variable hyperparameters of the MLP and their range are chosen from experience and

---

[17] $I_{ch,dr} = \{I_{ch,max}, I_{ch,mean}, I_{ch,SD}, I_{dr,min}, I_{dr,mean}, I_{dr,SD}\}$ with the BEV modes "ch" as charging and "dr" as driving.

are shown in Table 10. The constant hyperparameters of the MLP are the optimizer Adam, 300 epochs, MSE as loss function, ReLU activation function of the hidden layers,[18] and a linear activation function of the output layer. Early stopping is applied so that training stopped earlier than 300 epochs if the validation error did not decrease for more than 10 epochs. Version 2.8.0 of TensorFlow is used as back-end including version 2.8.0 of Keras.

Table 10: Overview of the used hyperparameters of the MLP during hyperparameter optimization.

Hyperparameter		Values
Batch size		32, 64, 128
Learning rate α		log-uniform distribution $[0.0001, 0.01]$
Number of layers		uniform distribution $[1, 15]$
Neurons per layer		log-uniform distribution $[20, 500]$
Choose one, others are 0:	Regularization parameter λ_1 or λ_2	log-uniform distribution $[0.001, 0.1]$
	Dropout rate	log-uniform distribution $[0.1, 0.5]$

5.2   Evaluation of Model Performance

We first evaluate the results of the models trained with histogram-based features in Section 5.2.1 and then with the accessible features in Section 5.2.2. Section 5.2.2 concludes with a comparison of both feature types. The hyperparameter optimization of the MLP never converges choosing the maximum of the value range in Table 10. This underlines a suitable choice of the value range of the hyperparameters.

For model comparison trained on data sets with different w_w, we use R^2 instead of the root mean squared error (RMSE) because w_w changes the output value distribution (ΔSOH) and R^2 normalizes the error by the variance of the output value distribution. R^2 represents the percentage of variance explained by the model. The highest possible score is 1.0. A score of 0.0 means that the model is as good as predicting the mean of the output values.

We define two criteria for model evaluation: First, the standard deviation (SD) σ of the model's performance on the data sets $s \in S = \{training, validation, test_1, test_2\}$ shall be small to avoid overfitting:[19]

$$\sigma = \sigma_{R_S^2} < 0.1 \text{ or } \sigma_{RMSE_S} < 0.1 \text{ %-}SOH \tag{8}$$

Second, if fulfilling the first criterion the mean μ of the model's performance on training, validation, and both test data sets shall be minimal:

$$\min \mu_{R_S^2} \text{ or } \min \mu_{RMSE_S}. \tag{9}$$

We refrained from a comparison to state-of-the-art models, like those listed in our previously published literature review [12], because of different data sets, different forecast horizons, different metrics, and different output values used, which limit comparability [12]. Thus, comparisons are limited to the same output value (ΔSOH) and the same data set only by variation of one parameter like the forecast horizon (w_w) and different input features describing the battery operation.

5.2.1   Histogram-based Features

The histogram-based features experiments are executed to analyze the effect of the following parameters on the model performance: The window width w_w, window shift w_s, signal interval width, histogram dimension, and separate histograms for each BEV mode.

---

[18] Rectified linear unit (ReLU) refers to a neuron that employs the rectifier activation function.

[19] With $\sigma_{R_S^2} = \sqrt{\frac{1}{|S|} \sum_{s \in S} \left(R_s^2 - \mu_{R_S^2} \right)^2}$ and $\sigma_{RMSE_S} = \sqrt{\frac{1}{|S|} \sum_{s \in S} \left(RMSE_s - \mu_{RMSE_S} \right)^2}$ as well as the corresponding $\mu_{R_S^2} = \frac{1}{|S|} \sum_{s \in S} R_s^2$ and $\mu_{RMSE_S} = \frac{1}{|S|} \sum_{s \in S} RMSE_s$ respectively where R_s^2 and $RMSE_s$ are R^2 and $RMSE$ on the respective data set s.

Experiment 1: Window Width w_{w}

The results of the models with a single window width are visualized in Figure 8. For all plots, the dotted red line in the lower plot indicates the upper limit for the SD of the R^2 from the first evaluation criterion.

For models trained on a data set with a small w_{w} like 1 EFC and 5 EFC, the first criterion is fulfilled ($\sigma_{R_S^2} < 0.1$), but the mean performance $\mu_{R_S^2}$ is low with only 0.045 and 0.172 respectively. This is likely caused by the bigger resolution of the SOH signal, 0.36 % in Table 6, compared to the small ΔSOH during few EFCs, 0.0173 % per EFC and vehicle of the whole fleet. This confirms the problem of small ΔSOH during few EFCs that also appeared with laboratory battery cell data in our previous work [23]. Thus, small w_{w} are not suitable due to low model performance.

For larger w_{w} like 25 EFC, 50 EFC, and 100 EFC, we observe overfitting as $\sigma_{R_S^2}$ increases gradually which is especially caused by a decreasing R^2 on the 2$^{\text{nd}}$ test data set, while R^2 of the training, validation, and 1$^{\text{st}}$ test data only move apart a little. This means for larger w_{w} that the ability to predict on new vehicles in the fleet is smaller than for vehicles whose data was used during training. By adjusting w_{s} in the next experiment the overfitting on the 2$^{\text{nd}}$ test data set shall be addressed. Overall, larger w_{w} show an increased performance on their training, validation, and 1$^{\text{st}}$ test data than smaller w_{w}.
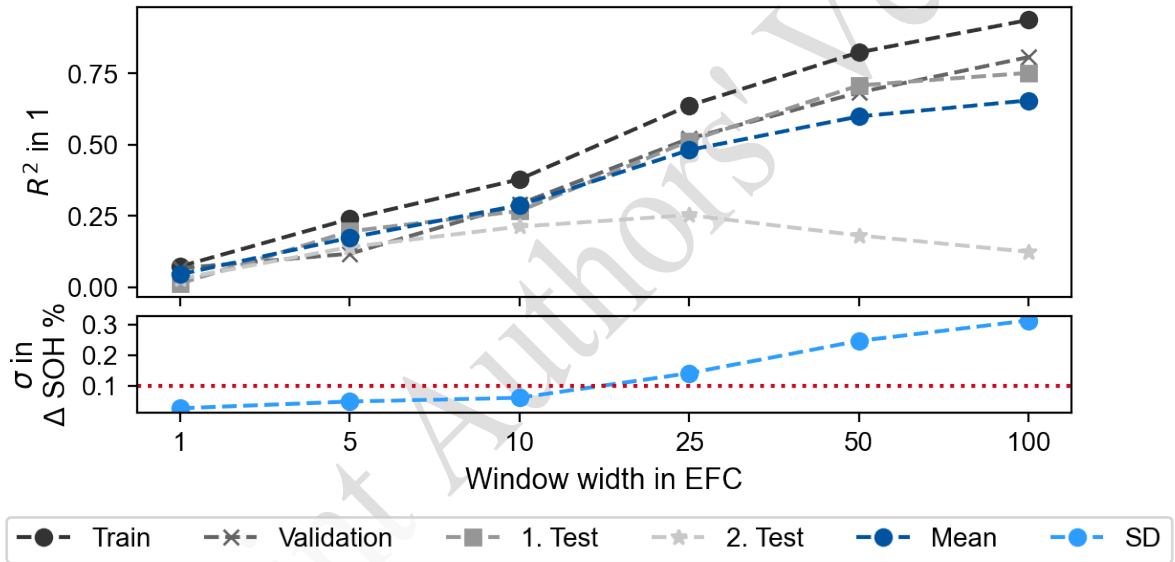

Figure 8: Model performance with different window widths w_{w} and histogram-based features.

In our previous work with laboratory battery cell data [23], combining different w_{w} improved model and generalization performance compared to the models with the corresponding single w_{w}. The same comparison is made in Table 11 for vehicle battery system data: We observe a reduction of SD over all data sets, but also a decrease of R^2. For example, for $w_{\text{w}} = \{25, 50, 100\}$ SD decreases by 29.3%, but also $\mu_{R_S^2}$ decreases by 7.2 %. We assume that due to the higher variability in the data from real-world vehicle operation compared to laboratory operation models with single w_{w} are already less prone to overfitting. So there is no need to add further variability by combining w_{w} as it was for data from laboratory operation as in our previous work [23]. As model performance did not improve for combining w_{w}, we do not consider combined w_{w} further, but try to improve generalization performance by adapting w_{s} in experiment 2.

Table 11: Model performance with combined window width w_w and histogram-based features

Window width w_w	$\{10, 25\}$	$\{25, 50\}$	$\{50, 100\}$	$\{10, 25, 50\}$	$\{25, 50, 100\}$
σ_{R^2}	0.132	0.2269	0.3483	0.2361	0.2218
μ_{R^2}	0.4267	0.5721	0.6061	0.536	0.607
Window width w_w	25	50	100	50	100
σ_{R^2}	0.1406	0.2468	0.3139	0.2468	0.3139
μ_{R^2}	0.4807	0.5986	0.6547	0.5986	0.6547

Experiment 2: Window Shift w_s

For the better performing $w_w \in \{10, 25, 50, 100\}$ from experiment 1, w_s was varied with the results displayed in Figure 9. The dotted red line again visualizes the limit for SD defined in the first evaluation criterion. In this experiment for constant w_w, varying w_s are compared in each subplot of Figure 9 so the output value distribution does not change. Thus, the RMSE is used as performance metric. Comparing results from different w_w, i.e., different subplots of Figure 9 is only possible with limitations considering the different forecast horizons.

For all w_w in Figure 9 there exists an optimal w_s minimizing the SD of the RMSE on the training, validation, and both test data sets (1st evaluation criterion). These optimal combinations of w_w and w_s are chosen for the following experiments: $(w_w, w_s) \in \{(10, 5), (25, 10), (50, 25), (100, 25)\}$. These pairs fulfill the 1st evaluation criterion and are best regarding the 2nd evaluation criterion in their group.
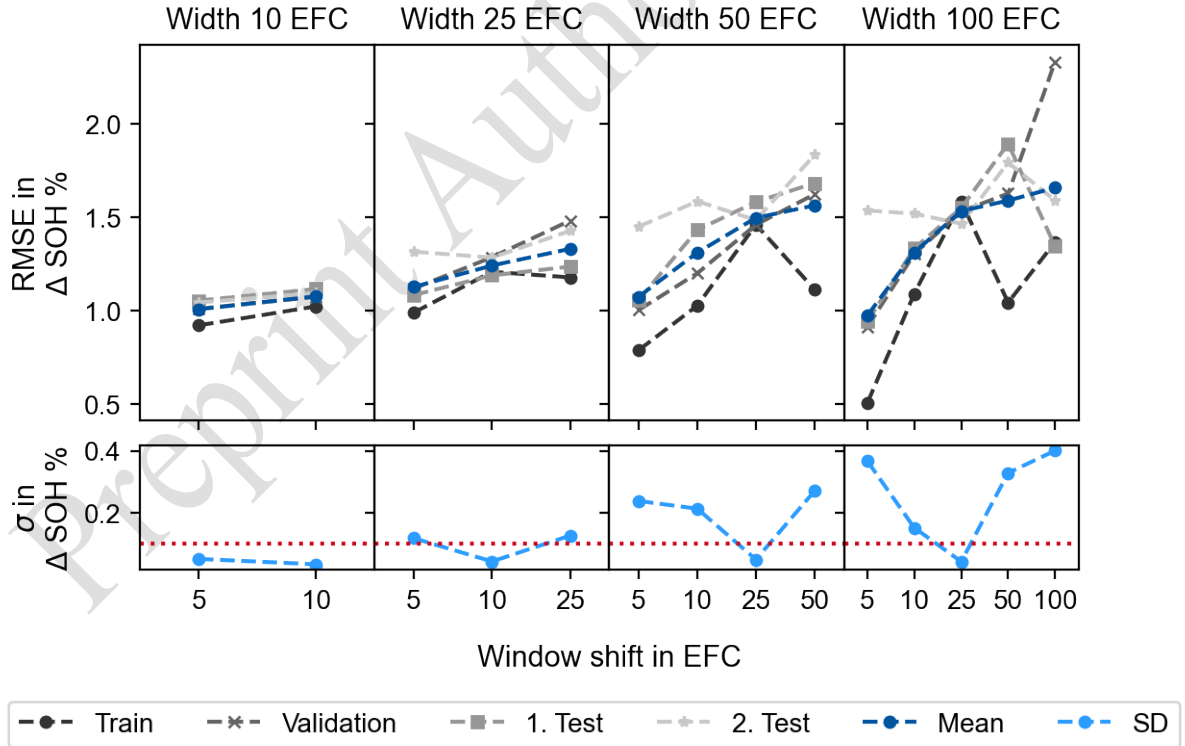
Figure 9: Model performance with different window shift w_s and histogram features

In the DOE in Section 5.1.1, we stated that w_s impacts the amount of training samples and the difference between training samples due to overlapping time ranges of two neighboring windows. To analyze the second aspect in more detail, we introduce the feature disparity: The feature disparity is the mean difference of each histogram feature value between neighboring windows of the same vehicle in the

data set. I.e., the mean is calculated over all histogram features, all pairs of neighboring windows, and all vehicles. The feature disparity is zero for the same window, i.e., the same histogram feature values ($w_s = 0$), close to zero for highly similar windows, and increasing the more dissimilar the histogram feature values are. As visualized in Figure 10, for increasing w_s the feature disparity increases independently of w_w because time windows overlap less.
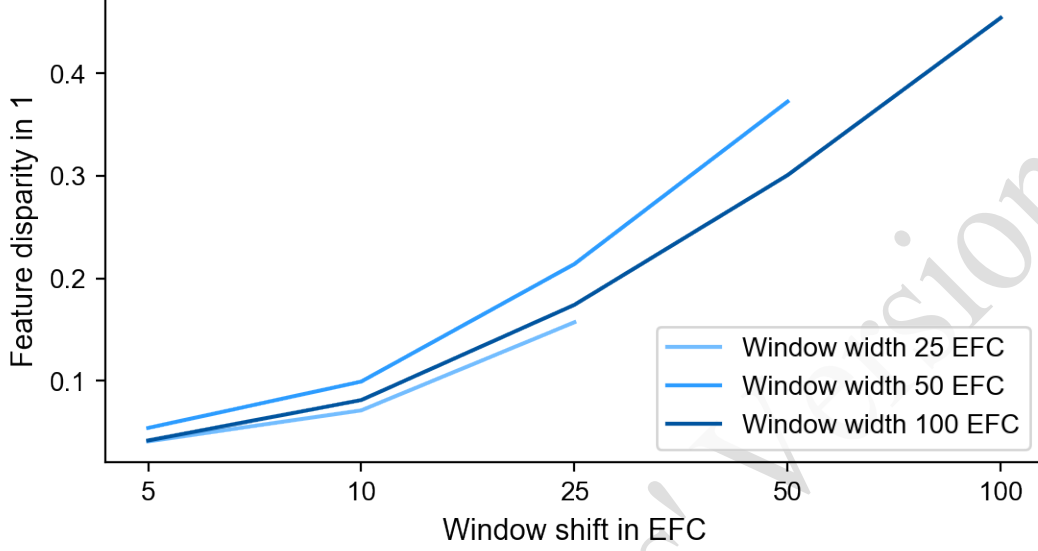

Figure 10: Histogram feature disparity over window shift w_s for several window width w_w

To analyze the potential dependence of the feature disparity on the model performance and generalization, Figure 11 depicts the model performance over the histogram feature disparity for all window shifts w_s and window widths w_w run in experiment 2. At low feature disparities between 0.0 and 0.1 there is a high variance of R^2 reaching a minimum around a feature disparity of 0.2 and increasing for higher values. The mean of R^2 increases from a feature disparity of 0.0 until reaching a plateau at around 0.1. Thus, we conclude that a feature disparity of around 0.2 offers a good trade off in-between model performance and generalization on training, validation, and both test data sets. Especially the performance on the 2nd test data set also reaches its maximum at a feature disparity of around 0.2. This also means that w_s is an effective means to control overfitting of the models. This holds especially true for the 2nd test data set which was sometimes not well-fit in experiment 1. With a feature disparity of around 0.2 as reference point for new data sets computationally expensive training and optimization of multiple models may be reduced. Nevertheless, this hypotheses needs to be further evaluated in future experiments.
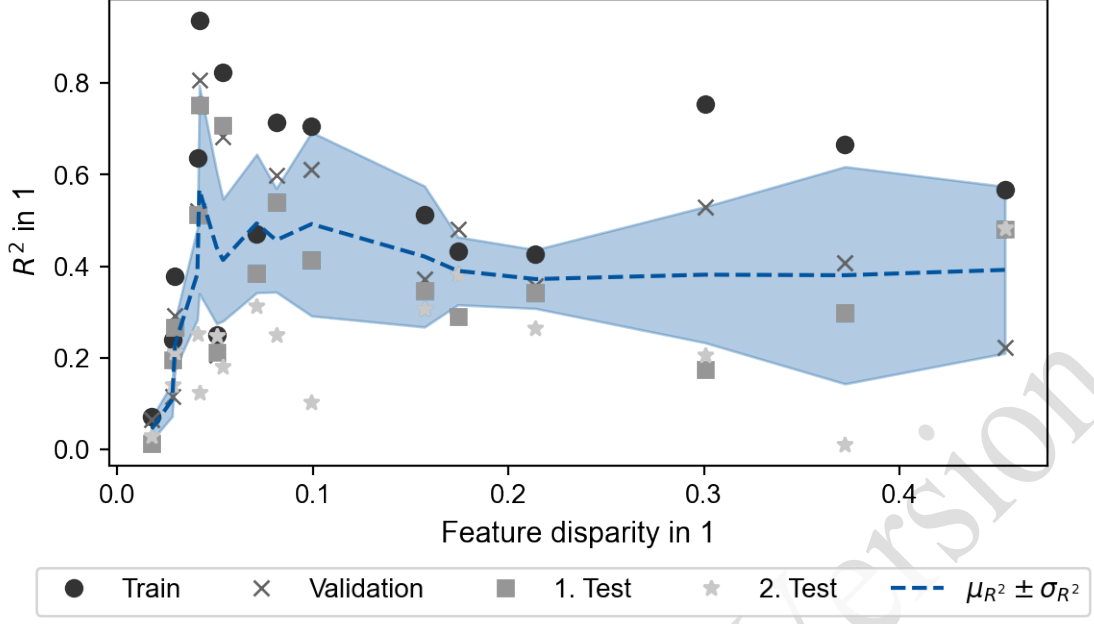
Figure 11: Model performance over histogram feature disparity for all window shift w_s and window width w_w run in experiment 2.

Experiment 3: Signal Interval Width

As shown in Figure 12, a finer signal interval width increases the SD for most models because only the RMSE on the training data improves. This is indicating an increasing overfitting. With a finer signal interval width the number of features increases from 369 for coarse, to 958 for medium and 3760 for fine but the number of samples is constant. This is problematic because it raises the curse of dimensionality: An exponentially increasing number of training samples is required to cover an increasing number of features and their combinations [145]. Furthermore, the ML models have +10 % parameters for medium and +249 % for fine compared to coarse signal interval width which is not dampened by regularization so the models overfit. We opt to continue with the coarse signal interval width in the next experiments because only the coarse signal interval width satisfies the first evaluation criterion for all w_w.
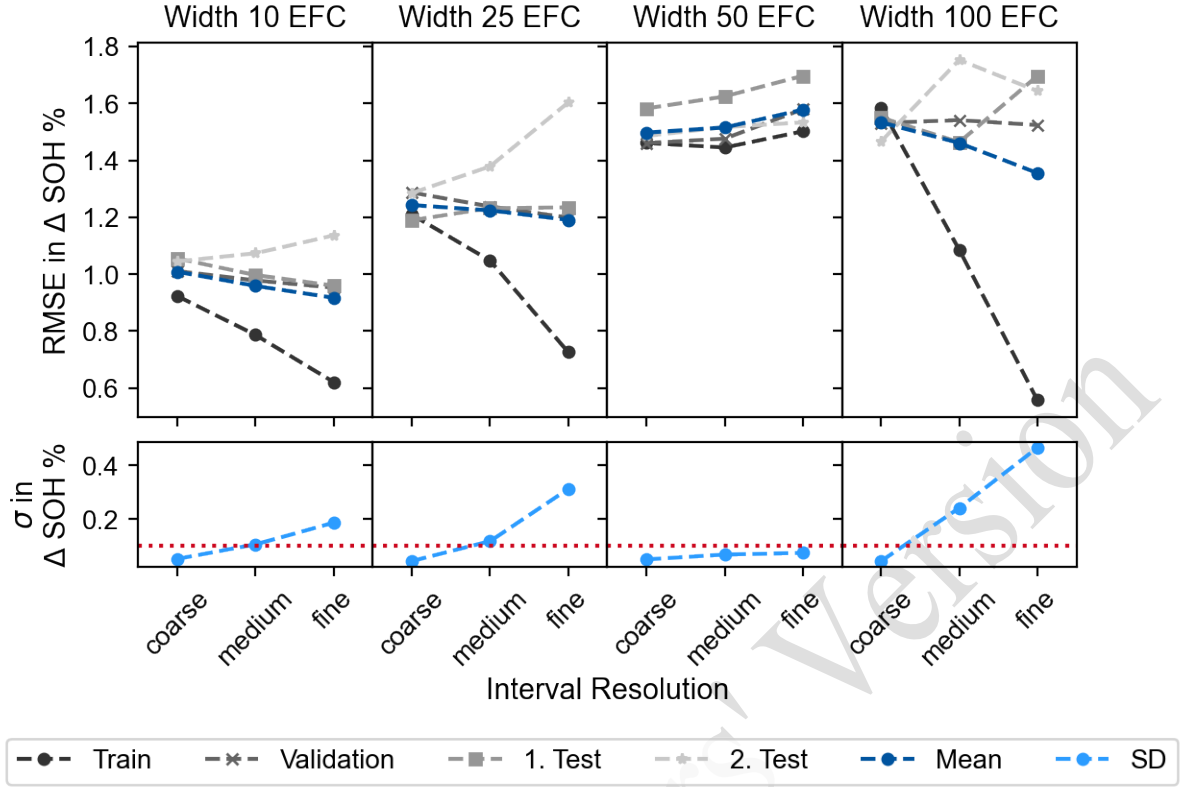
Figure 12: Model performance with different signal interval widths and histogram features

Experiment 4: Histogram Dimension

Similar to experiment 3, when increasing the histogram dimensions in this experiment, the number of features increases from 67 for 1D up to 369 for 2D and 1153 for 3D histograms. In Figure 13 the corresponding results are visualized. For w_w as 10, 25, and 50 cycles the 1st evaluation criterion regarding SD is fulfilled independently the histogram dimension. However, for $w_w = 100$ cycles the 1st evaluation criterion is only fulfilled for 2D histograms and for $w_w = 50$ cycles SD is still lower for 2D histograms than for 1D and 3D histograms. For $w_w \in \{10, 25, 50\}$ cycles, the mean RMSE on training, validation, and both test data sets improves by 0.016 % SOH when switching from 1D to 2D and decreases by 0.0036 % SOH when switching from 2D to 3D. So the differences for these w_w caused by the histogram dimension are minor. This is not the case for $w_w = 100$ cycles where the model overfits on the training data for 1D and 3D, similar to the medium and fine signal interval width in experiment 3.

In general, the 2D histograms seem to provide a good balance between a sufficient representation of battery aging causes and low number of features. Besides, editing 2D histograms for virtual predictions, i.e., what-if scenarios, is easier and more conceivable as 3D histograms which are difficult to represent visually.
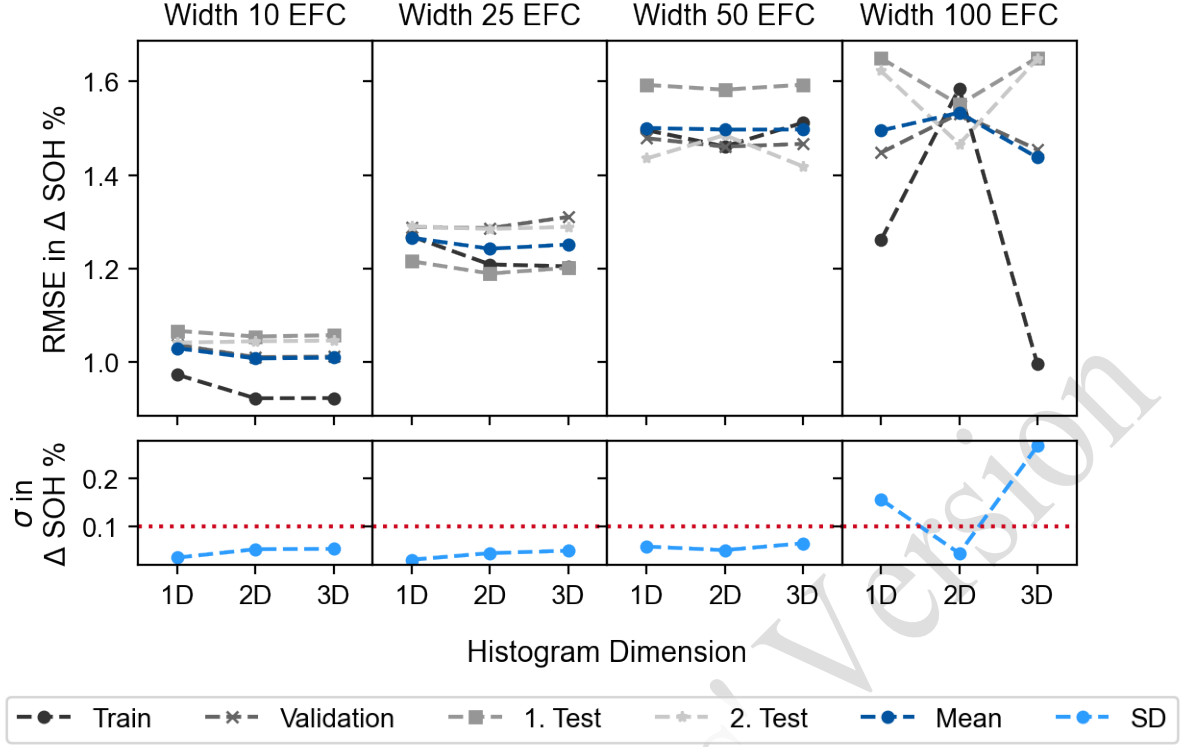
Figure 13: Model performance with different histogram dimensions

Experiment 5: Separation of BEV Modes

The separation of histograms by the BEV mode barley influences the model performance for $w_w \in \{10, 25, 50\}$ cycles as the results in Figure 14 show. As in the previous experiments, for $w_w = 100$ cycles the performance is more variable: When separating charging into AC- and DC-charging (B) compared to no separation at all (A) the SD increases by 219 % and the mean RMSE decreases by 1.4 %. The small mean RMSE improvement may be explained by only little information added by separating the charging modes. Already the current alone offers enough potential for differentiation of AC- and DC-charging in the histograms. In particular for the final phase at the end of DC-charging, especially the CV phase, when the current is controlled and as low as for AC-charging separate histograms for AC- and DC-charging (B) offer additional information.

Without BEV mode differentiation (C) the SD increases by 95 % and the mean RMSE increases by 1 % compared to A. Thus, we conclude that separate histograms by the BEV modes charging, driving, parking (A) are preferable and select this variant for the final models. Furthermore, this allows explicit distinction of different BEV modes during the model application.
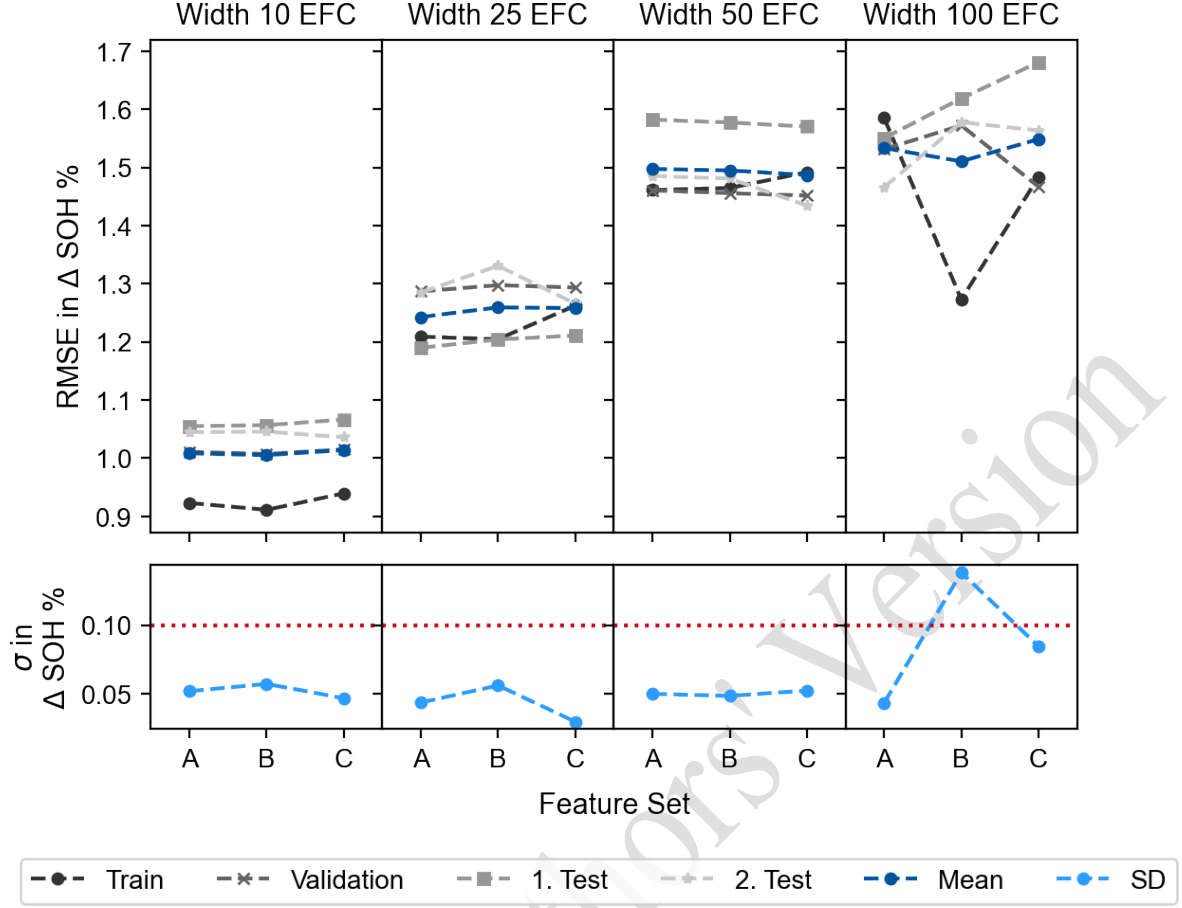
Figure 14: Model performance considering BEV-modes separately

The final models selected after experiment 5 and their hyperparameters are summarized in Table 14.

Exemplarily, for the model trained on $w_w = 25$ and $w_s = 10$ Figure 15 shows the $\Delta SOH_{\text{predicted}}$ over the $\Delta SOH_{\text{measured}}$. The RMSE of all four data sets, training, validation, 1. Test, and 2. Test, is very similar (SD of only 0.043, see Table 16). A qualitative comparison of these plots with the same method applied on battery cell data from laboratory operation as in [23] shows that SOH forecasting with the given real-world battery system data performs worse. We expect these results to become better with finer time series data sampling and more precise SOH labels.
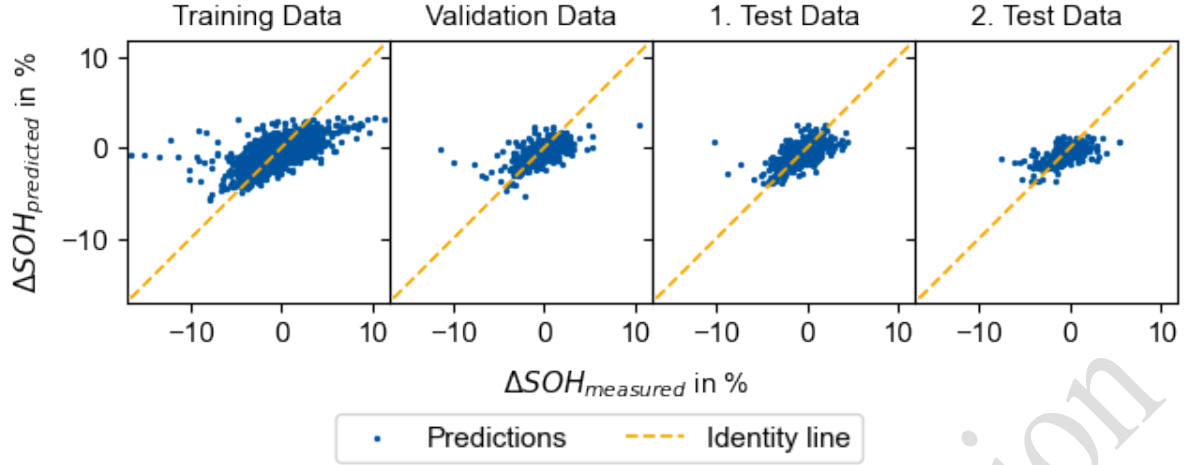
Figure 15: Model performance after last experiment, model H2 ($w_w = 25$ and $w_s = 10$), $\Delta SOH_{predicted}$ over the $\Delta SOH_{measured}$. The corresponding RMSE values are: 1.209, 1.287, 1.189, and 1.285 respectively (Training, Val, 1. Test, 2. Test).

The same predictions as in Figure 15 are displayed as moving boxplot compared to the mean measured SOH in Figure 16. Also, the 50 % and 90 % confidence zone for the prediction error are visualized which represent the upper and lower boundaries of the 50 % and 90 % best predictions respectively compared to the mean SOH curve. Until around 300 EFC the 50 % confidence zone has a width of around 1 % SOH. This means half of the predictions deviate less than 0.5 % SOH from the measured SOH. The 90 % confidence zone is significantly wider with around 3.5 % SOH. After around 300 EFC there are too few data samples available which explains the arbitrary mean SOH curve, i.e., predictions after that point in time should not be considered as valid.
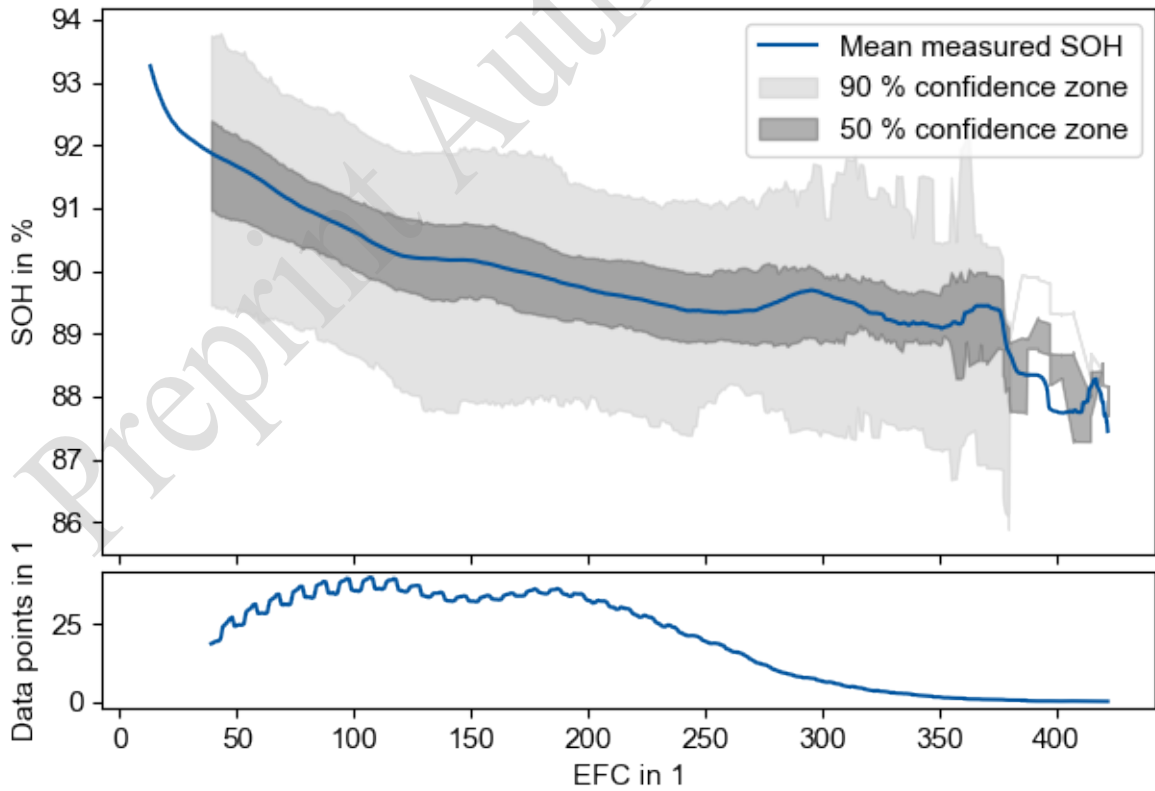

Figure 16: SOH forecasting error of the whole fleet with model H2 ($w_w = 25$ and $w_s = 10$). The characteristics of the mean measure SOH have been discussed at Figure 4 already.

5.2.2 Accessible Features

For an initial assessment of the accessible features, Figure 17 depicts a boxplot diagram of the variance of the accessible features after min-max-normalization. The feature $\Delta k = w_\mathrm{w}$ is always the same for single, i.e., non-grouped w_w, because the sliding window procedure is oriented at EFCs and not, e.g., at the total operational time, e.g., with $w_\mathrm{w} = 30\,d$. The features $I_{\mathrm{ch,max}}$ and SOE_{max} have a very low variance because their maximum value is always reached at some point during battery operation, either at DC charging or after a complete charging session to $SOE = 100\,\%$ respectively. We expect these features to offer only little potential for differentiation of the samples during model training.
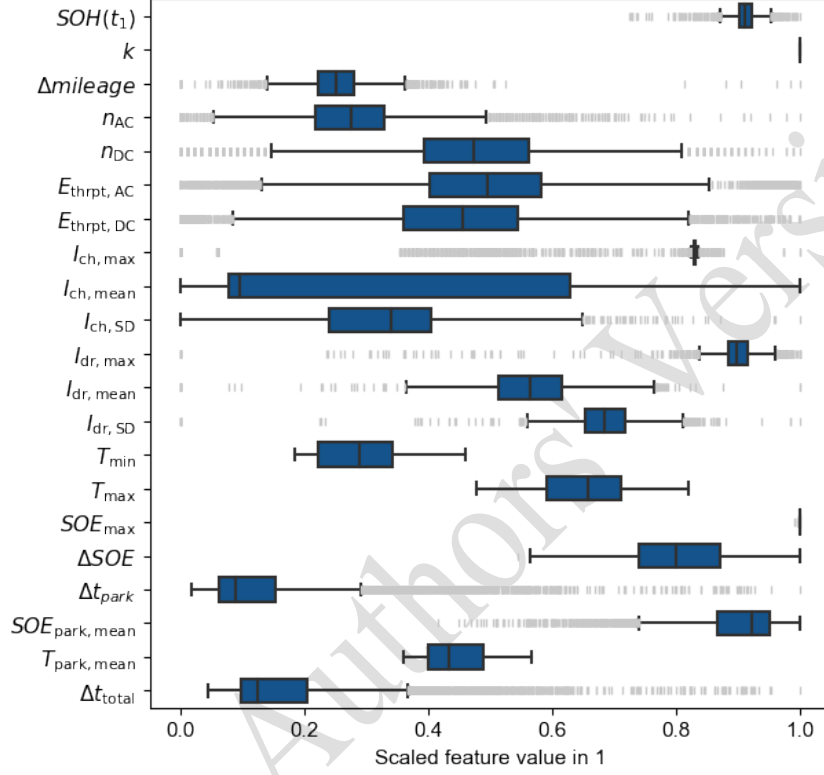

Figure 17: Variance of the accessible input features after min-max-normalization for $w_\mathrm{w} = 25$ and $w_\mathrm{s} = 10$.

Experiment 1: Window Shift w_s

Figure 18 depicts the model performance only with $SOH(t_1)$ as accessible feature for combinations of w_w and w_s. The model performance is quite similar for different w_s. Based on the evaluation criteria we choose for the following experiments: $(w_\mathrm{w}, w_\mathrm{s}) \in \{(10, 5), (25, 10), (50, 10), (100, 10)\}$.
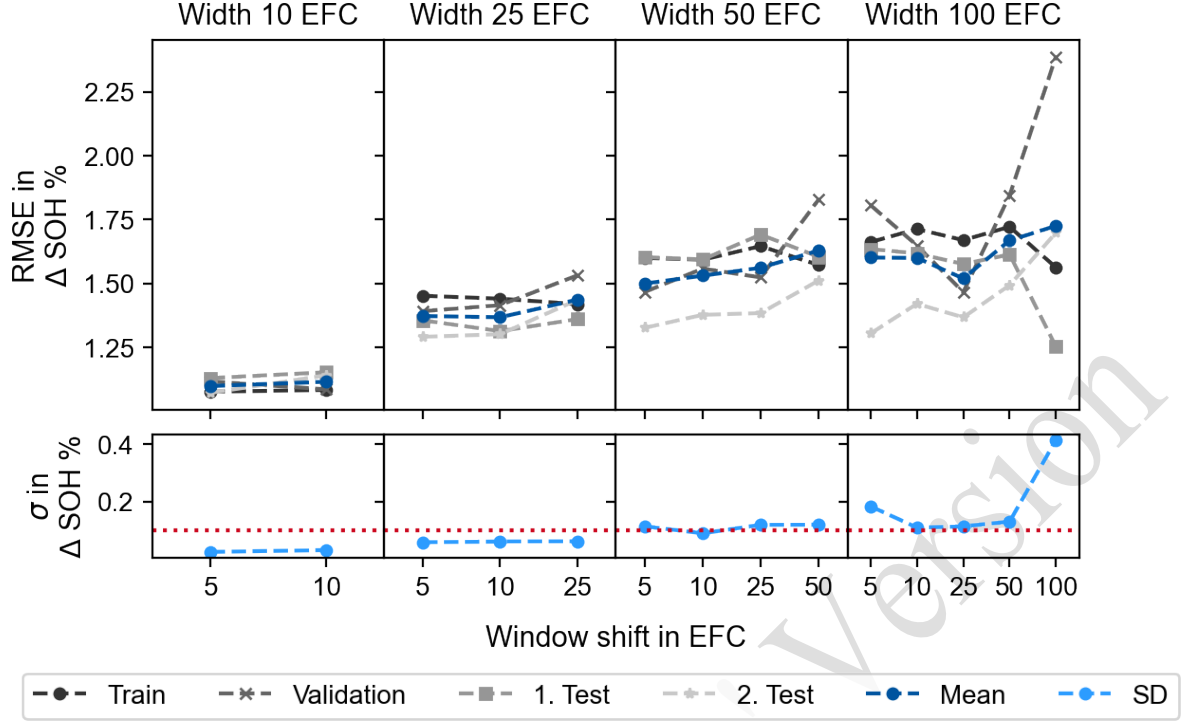
Figure 18: Model performance with different window shift w_s and only $SOH(t_1)$ as accessible feature

Experiment 2a: Cyclic Aging

The results of experiment 2a and 2b are compared to the base line of experiment 1 only with $SOH(t_1)$ as accessible feature. Figure 19 shows that the model performance with additional accessible features improves slightly. As for the histogram-based features SD increases for higher w_w, like $w_w = 100$ cycles. Feature sets 2a.4 and 2a.5 are performing best concerning the evaluation criteria ($E_{\text{thrpt,AC}}$ &

$E_{\text{thrpt,DC}}$ and $I_{\text{ch,dr}}$ respectively). Furthermore, they show a minor improvement of the mean RMSE compared to the baseline feature set 1 by 2.5 % and 1.6 % respectively.
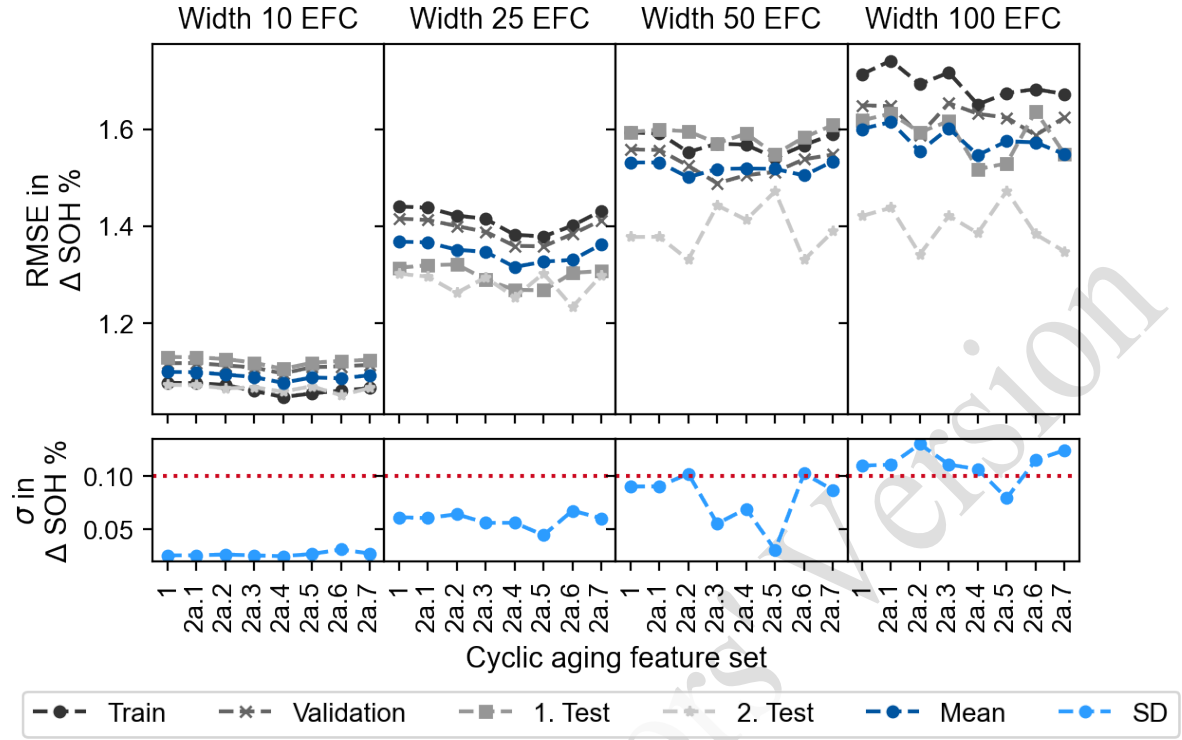

Figure 19: Model performance with accessible feature describing cyclic aging

Experiment 2b: Calendar Aging

As depicted in Figure 20, only the models trained on feature set 2b.4 fulfill the first evaluation criterion for all w_{w}. Also, for feature set 2b.4 (Δt_{total}) over all w_{w} the mean RMSE compared to the baseline feature set 1 decreases the most by 2.2 %. For feature sets 2b.1, 2b.2, and 2b.3, the decrease is only 1.5 %, 0.5 %, and 0.8 % respectively.
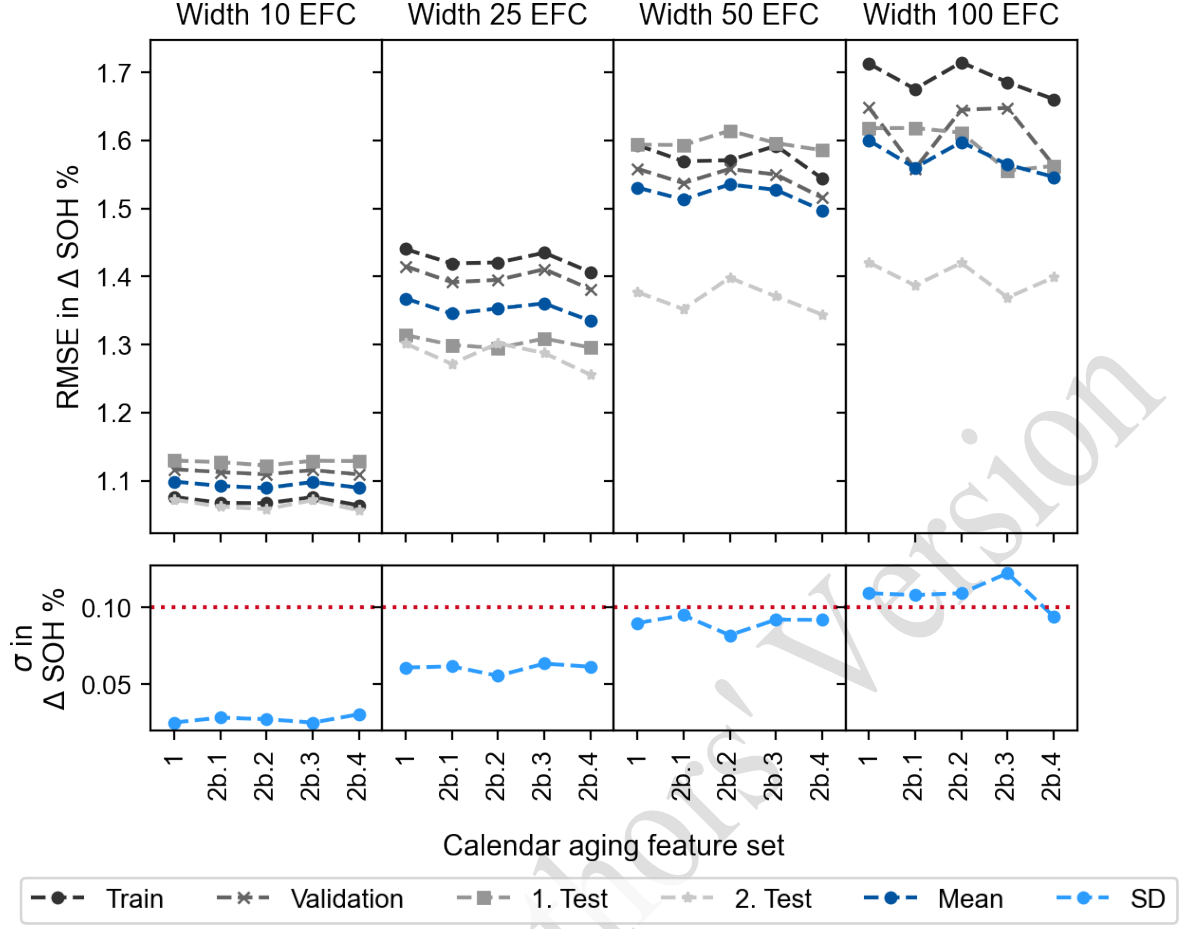
Figure 20: Model performance with accessible feature describing calendar aging

Experiment 3: Cyclic & Calendar Aging

As depicted in Figure 21, when using all features from experiment 2a and 2b as feature set 3.1, the threshold of the first evaluation criterion exceeds for $w_\mathrm{w} = 50$ cycles. Using only the selected features ($E_\mathrm{thrpt,AC}$, $E_\mathrm{thrpt,DC}$, $I_\mathrm{ch,dr}$, Δt_{total}) from experiment 2a and 2b, together with the $SOH(t_1)$ in feature set 3.2 results in lower SD and improves the mean RMSE over the baseline feature set 1 over all window widths by 3.8 %.
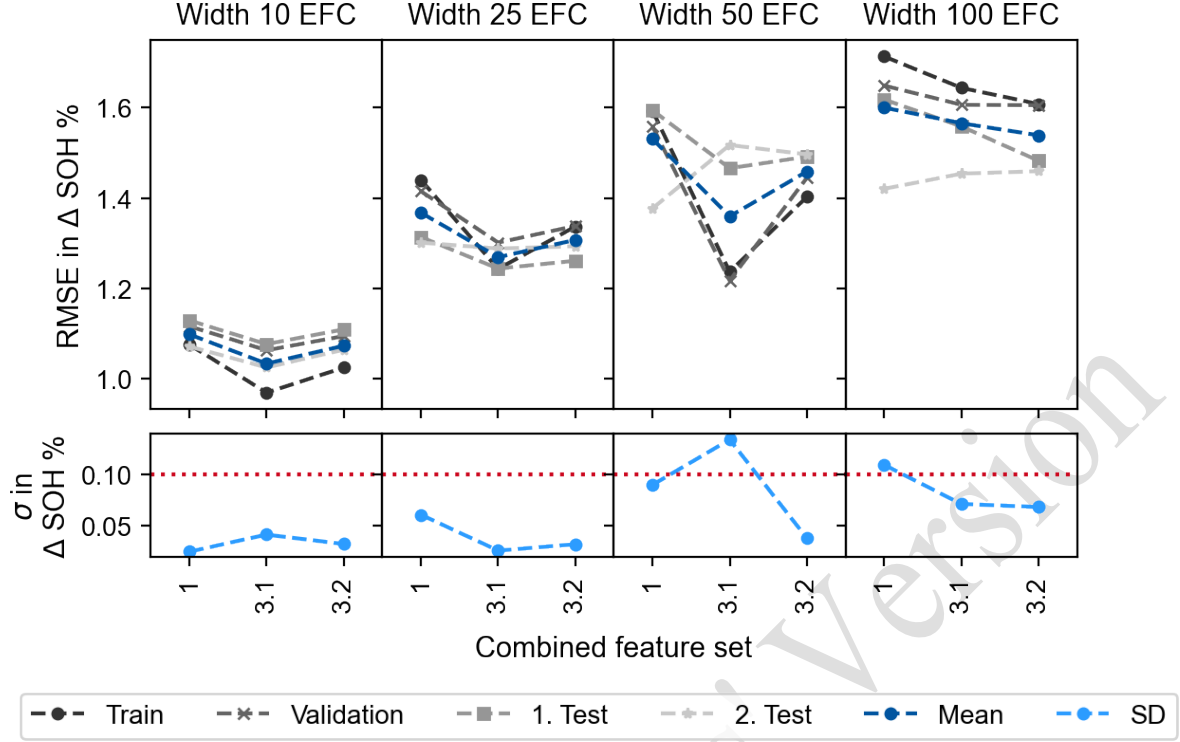
Figure 21: Model performance with accessible feature describing cyclic and calendar aging

Comparison of Histogram-based and accessible Features

Feature set 3.2 has only ten input features, which is significantly less than the 369 features of the histogram-based approach. Despite, the number of model parameters is roughly in the same dimension of 10^5, i.e., the model complexity is not always reduced. On average the mean RMSE is 2 % better for the histogram-based features compared to the accessible features over all w_w as listed in Table 16 in the Appendix. For a high w_w of 100 EFCs, the performance is similar because the operational load encoded in the histograms is smoothed strongly given the large aggregated time window. I.e., the operational load in the windows becomes similar. For smaller w_w of 10 and 25 EFCs, the histogram-based features are better than the accessible features (6.1 % and 5.0 % respectively). Thus, we conclude that histogram-based features are preferable as they offer more detailed encoding and aggregation of battery operational load.

5.3 Use cases

To exemplarily demonstrate how the SOH forecasting model could be applied, e.g., by fleet managers as mentioned in the introduction, we create two practical and easy to understand use cases that are applied to the model with histogram-based features (H2). For each use case the battery operational test data of the fleet is modified according to a scenario as introduced in Section 2.3. Therefore, the input data was fed to the model iteratively: The $SOH(t_1)$ of the next time window was calculated as $SOH(t_1) + \Delta SOH$ of the previous time window with ΔSOH as the model output. A drawback of this procedure is that the prediction error accumulates and the prediction performance decreases by time. However, it allows to show the long term effect of the modified scenario data. All results in this section need to be interpreted carefully because the interfered results shown in the plots are only expressing what the ML model has learnt, not necessarily how the aging really would have been. It is important to ensure that the ML model does not extrapolate.

Charging Management: Limitation of $SOE_{park,max}$

We assume that an intelligent charging management was employed to limit the maximum SOE at the end of a charging session. This reduced SOE during the following parking may lead to decelerated

calendar aging. The mean SOE during parking for the baseline is at 90 % so that a limitation of $SOE_{\text{park,max}}$ to 90 % would only change the time series data a little. Furthermore, for the coarse signal interval width of 20 % these values would all remain in the same bin. Thus, it is not shown in Figure 22. Compared to the unmodified baseline, a $SOE_{\text{park,max}}$ limit of 80 % does not change the fleet's aging much. However, for a $SOE_{\text{park,max}}$ limit of 60 % the aging is significantly reduced. E.g., around 150 EFC the SOH is 0.8 % SOH smaller compared to the baseline. From there until 300 EFC the difference reduces, potentially because parking becomes less dominant after the breaks caused by COVID-19. The influence of limiting $SOE_{\text{park,max}}$ learnt by the model and observed in this scenario corresponds to the results of Keil et al. [146] who find in laboratory cell experiments that calendar aging shows plateaus with SOE intervals of 20 % to 30 % with similar degradation, i.e., a non-linear dependency of SOE and calendar aging.
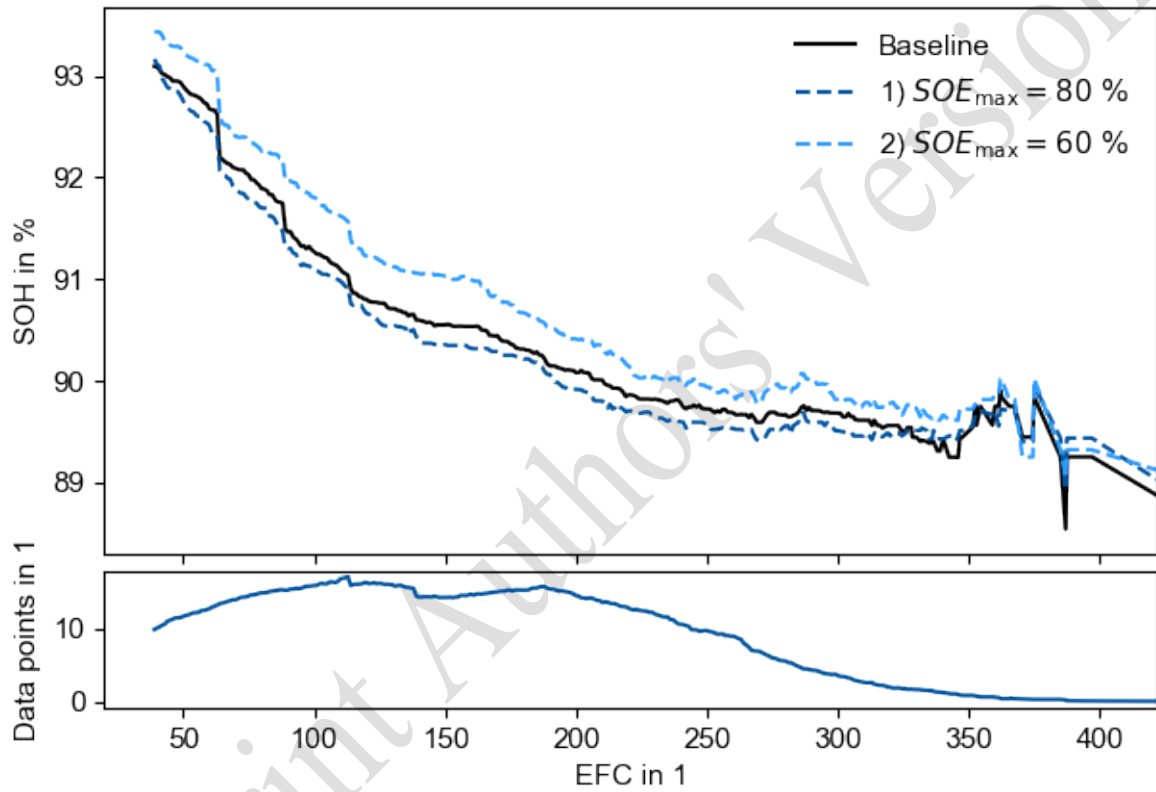

Figure 22: Fleet SOH forecasting with scenario of limited $SOE_{\text{park,max}}$ and model H2.

Charging Management: Only AC-charging

In laboratory cell experiments it was observed that high C-rates accelerate battery aging [45,46]. In vehicle operation, high C-rates may occur during DC-charging, especially during high power charging (HPC). Figure 23 shows the fleet aging trajectory of the unmodified baseline scenario with a mixture of AC- and DC-charging. When assuming AC-charging by limiting the C-rate, the SOH increases by about 0.1 % SOH which we consider negligibly small. However, the DC-charging C-rate was only around 1.25C during DC-charging, so relatively low compared to battery cell experiments with up to 8C [84,85]. Also, it has to be noted that for switching from AC- to DC-charging the duration of the charging session, temperature, and SOE would change. This was not done in this scenario so that only the influence of changed current distribution is considered, i.e., ceteris paribus. Further influences, e.g., of charging at lower and high temperatures were not considered in this use case.
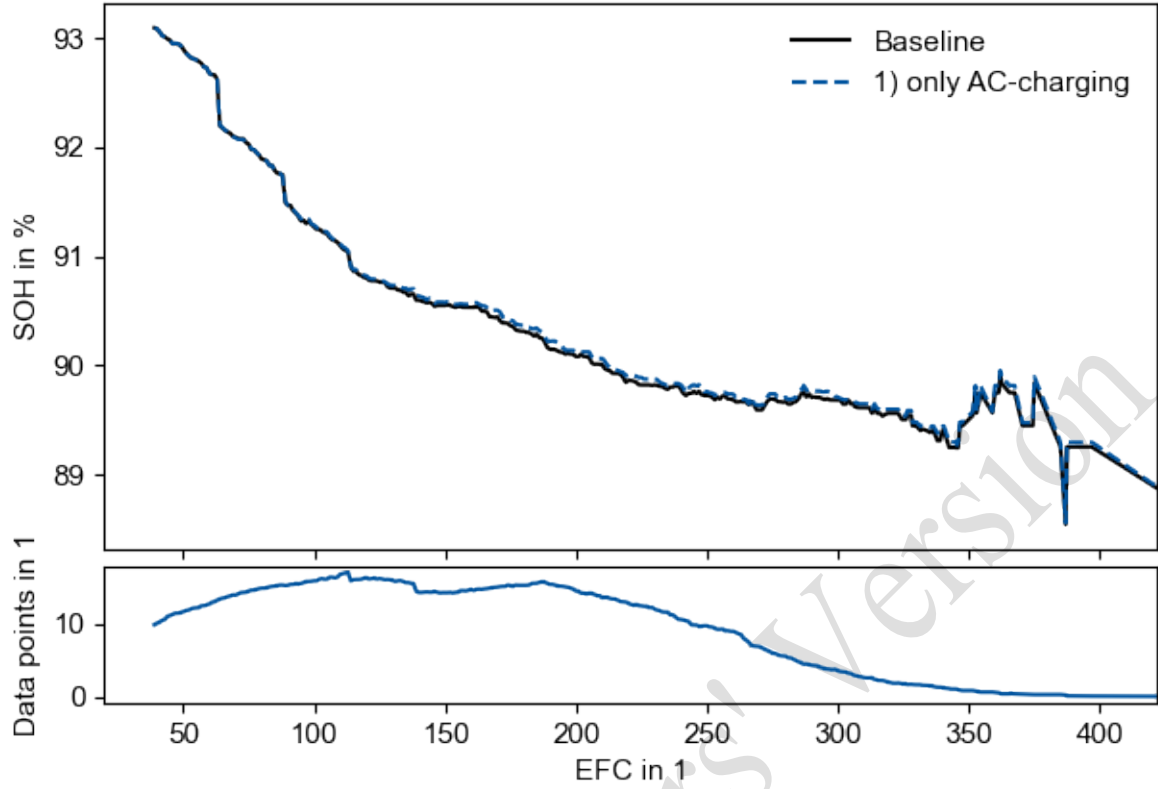
Figure 23: Fleet SOH forecasting with scenario of only AC-charging and model H2

6 Conclusion

Our previous work [17,23] has shown that SOH forecasting works with laboratory battery cell data. In this work, this existing SOH forecasting method based on histogram features was successfully applied to battery system data from the real-world BEV fleet operation of a ride-pooling MOD provider. The model was able to learn the dependence of the SOH from the battery load, i.e., BEV usage. Compared to the laboratory battery cell data the generalization of models trained on vehicle system data did not improve when learning multiple forecast horizons (w_w). In addition, overfitting on newly joined vehicles was controllable by the number of samples generated (w_s). Two use cases for different charging strategies illustrate how the SOH forecasting model may be applied. Switching from accessible features to the histogram-based features showed an improvement in model performance of up to 6.1 %.

The model is mainly limited by the data used for training in several ways: First, the measurement accuracy and sampling rate of the battery signals can limit the performance of the model, especially of the SOH signal and temperature signal during parking. Second, the method assumes path independence of battery aging, i.e., the order of operational states encoded in the histograms does not matter [147,148]. Third, the current state representation is assumed to be accurately represented only by $SOH(t_1)$, i.e., no other features such as $E_{\mathrm{thrpt}}(t_1)$ are used. Likewise it is assumed that the load applied to the battery before t_1 is either already reflected by $SOH(t_1)$ or does not affect the SOH trajectory after t_1. Furthermore, no mechanical or vibrational stress is considered which also affects battery aging [149,150]. Third, since the model is purely data-driven it may only provide good interpolations within the range of the training data.

In future work it seems beneficial to build a hybrid model that combines empirical knowledge from laboratory experiments with features that can encode the variability of real-world vehicle operation. Alternatively, a model pre-trained on laboratory battery cell data of the same cell type build in the BEV's battery system may provide a good starting point for transfer learning to the battery system operated in real-world conditions. Transfer learning utilizes knowledge previously acquired in one domain to solve a task in a novel domain [151]. Battery domains could be specified by their operational

load, the operational region, the battery type used, and the configuration of the battery system or as a single cell [24].

Going beyond the assumption that a single value is capable of characterizing the state of a battery with respect to its aging, the SOH could be extended from a single value like the capacity, storable energy, or resistance to a vector of multiple values which could also consider capacity recovery effects more accurately. With a single-value based SOH, in the case of capacity recovery a battery in two different situations and contexts could have the same SOH which is not desired.

Assuming system-level and cell-level data of BEV battery systems, the interdependencies of current, temperature, and SOE on battery aging when switching from cell to pack as discussed in Section 2.1.2 may be considered in more detail. For example, by considering the temperature not only at the system-level, but also at the cell-level or module-level as well may enable a SOH forecasting model to consider a SOH distribution in the battery system. Interdependencies within systems like industrial cool boxes [152] and gearbox systems [153] have been modeled by a dependency matrix to express the interaction of the components in a multicomponent system [154]. This has not yet been done for batteries, but it seems possible given the construction plan of a battery system.

Author Contributions

Credit author statement:

Friedrich von Bülow: Conceptualization, Methodology, Software, Investigation, Visualization, Writing - Original Draft, Writing - Review & Editing

Markus Wassermann: Software, Investigation, Visualization, Writing - Review & Editing

Tobias Meisen: Writing - Review & Editing

Competing Interests Statement

The authors declare that they have no known competing financial interests or personal relationships that could have appeared to influence the work reported in this paper.

Disclaimer

The results, opinions and conclusions expressed in this publication are not necessarily those of Volkswagen Aktiengesellschaft.

Data Availability

The data generated during and/or analyzed in this work are not publicly available due to confidentiality reasons.

References

[1] S. Leuthner, Lithium-ion battery overview, in: R. Korthauer (Ed.), Lithium-Ion Batteries: Basics and Applications, Springer Berlin Heidelberg, Berlin, Heidelberg, Germany, 2018, pp. 13–19.

[2] A. König, L. Nicoletti, D. Schröder, S. Wolff, A. Waclaw, M. Lienkamp, An Overview of Parameter and Cost for Battery Electric Vehicles, WEVJ. 12 (2021) 21. https://doi.org/10.3390/wevj12010021.

[3] J. Miller, Electric car costs to remain higher than traditional engines. https://www.ft.com/content/a7e58ce7-4fab-424a-b1fa-f833ce948cb7, 2020 (accessed 1.03.2023).

[4] S. Su-hyun, [Chew on I.T.] What makes up smartphone prices? https://www.koreaherald.com/view.php?ud=20200607000076, 2020 (accessed 1.03.2023).

[5] A. Cowsky, Cost Comparison – Huawei Mate 10, iPhone 8, Samsung Galaxy S8. https://www.techinsights.com/blog/cost-comparison-huawei-mate-10-iphone-8-samsung-galaxy-s8, 2017 (accessed 1.03.2023).

[6] International Energy Agency (IEA), Global Electric Vehicle Outlook 2021. https://iea.blob.core.windows.net/assets/ed5f4484-f556-4110-8c5c-4ede8bcba637/GlobalEVOutlook2021.pdf, 2021 (accessed 1.03.2023).

[7] International Energy Agency (IEA), Global Electric Vehicle Outlook 2022. https://iea.blob.core.windows.net/assets/ad8fb04c-4f75-42fc-973a-6e54c8a4449a/GlobalElectricVehicleOutlook2022.pdf, 2022 (accessed 1.03.2023).

[8] StartUs Insights, 5 Top Battery Analytics Startups. https://www.startus-insights.com/innovators-guide/battery-analytics-startups/, 2022 (accessed 1.03.2023).

[9] J. Warner, The Handbook of Lithium-Ion Battery Pack Design, Elsevier, Amsterdam, The Netherlands, 2015.

[10] R. Dorn, R. Schwartz, B. Steurich, Battery management system, in: R. Korthauer (Ed.), Lithium-Ion Batteries: Basics and Applications, Springer Berlin Heidelberg, Berlin, Heidelberg, Germany, 2018, pp. 165–175.

[11] W. Waag, D.U. Sauer, SECONDARY BATTERIES – LEAD–ACID SYSTEMS | State-of-Charge/Health, in: J. Garche (Ed.), Encyclopedia of electrochemical power sources, Elsevier, Amsterdam, The Netherlands, 2009, pp. 793–804.

[12] F. von Bülow, T. Meisen, A review on methods for state of health forecasting of lithium-ion batteries applicable in real-world operational conditions, J. of Energy Storage. 57 (2023) 105978. https://doi.org/10.1016/j.est.2022.105978.

[13] F. Petropoulos, D. Apiletti, V. Assimakopoulos, M.Z. Babai, D.K. Barrow, S. Ben Taieb, C. Bergmeir, R.J. Bessa, J. Bijak, J.E. Boylan, J. Browell, C. Carnevale, J.L. Castle, P. Cirillo, M.P. Clements, C. Cordeiro, F.L. Cyrino Oliveira, S. de Baets, A. Dokumentov, J. Ellison, P. Fiszeder, P.H. Franses, D.T. Frazier, M. Gilliland, M.S. Gönül, P. Goodwin, L. Grossi, Y. Grushka-Cockayne, M. Guidolin, M. Guidolin, U. Gunter, X. Guo, R. Guseo, N. Harvey, D.F. Hendry, R. Hollyman, T. Januschowski, J. Jeon, V.R.R. Jose, Y. Kang, A.B. Koehler, S. Kolassa, N. Kourentzes, S. Leva, F. Li, K. Litsiou, S. Makridakis, G.M. Martin, A.B. Martinez, S. Meeran, T. Modis, K. Nikolopoulos, D. Önkal, A. Paccagnini, A. Panagiotelis, I. Panapakidis, J.M. Pavía, M. Pedio, D.J. Pedregal, P. Pinson, P. Ramos, D.E. Rapach, J.J. Reade, B. Rostami-Tabar, M. Rubaszek, G. Sermpinis, H.L. Shang, E. Spiliotis, A.A. Syntetos, P.D. Talagala, T.S. Talagala, L. Tashman, D. Thomakos, T. Thorarinsdottir, E. Todini, J.R. Trapero Arenas, X. Wang, R.L. Winkler, A. Yusupova, F. Ziel, Forecasting, Int. J. of Forecasting. 38 (2022) 705–871. https://doi.org/10.1016/j.ijforecast.2021.11.001.

[14] Münchener Rückversicherungs-Gesellschaft, Battery performance now insurable – Innovative Munich Re coverage paves the way for renewable energy. https://www.munichre.com/content/dam/munichre/contentlounge/website-pieces/documents/Munich-Re-PM-2019-03-07_en.pdf, 2019 (accessed 1.03.2023).

[15] Z. Zhou, A. Ran, S. Chen, X. Zhang, G. Wei, B. Li, F. Kang, X. Zhou, H. Sun, A fast screening framework for second-life batteries based on an improved bisecting K-means algorithm combined with fast pulse test, J. of Energy Storage. 31 (2020) 101739. https://doi.org/10.1016/j.est.2020.101739.

[16] A. Aitio, D.A. Howey, Predicting battery end of life from solar off-grid system field data using machine learning, Joule. 5 (2021) 3204–3220. https://doi.org/10.1016/j.joule.2021.11.006.

[17] R.R. Richardson, M.A. Osborne, D.A. Howey, Battery health prediction under generalized conditions using a Gaussian process transition model, J. of Energy Storage. 23 (2019) 320–328. https://doi.org/10.1016/j.est.2019.03.022.

[18] Y. Che, X. Hu, X. Lin, J. Guo, R. Teodorescu, Health prognostics for lithium-ion batteries, Energy Environ. Sci. 16 (2023) 338–371. https://doi.org/10.1039/d2ee03019e.

[19] O. Juhlin, Modeling of Battery Degradation in Electrified Vehicles. Master Thesis. Linköpings universitet, Linköping, Sweden, 2016. http://urn.kb.se/resolve?urn=urn:nbn:se:liu:diva-134114 (accessed 1.03.2023).

[20] D.U. Sauer, Einfluss der Batteriestreuung und Lebensdauer auf das Batteriesystemdesign, 2015 (accessed 1.03.2023).

[21] S. Shaheen, A. Cohen, Similarities and Differences of Mobility on Demand (MOD) and Mobility as a Service (MaaS), Institute of Transportation Engineers Journal: MaaS/MOD. 90 (2020) 29–35.

[22] S. Shaheen, A. Cohen, Chapter 3 - Mobility on demand (MOD) and mobility as a service (MaaS): early understanding of shared mobility impacts and public transit partnerships, in: D. Efthymiou, C. Antoniou, E. Chaniotakis (Eds.), Demand for Emerging Transportation Systems, Elsevier, 2020, pp. 37–59.

[23] F. von Bülow, J. Mentz, T. Meisen, State of health forecasting of Lithium-ion batteries applicable in real-world operational conditions, J. of Energy Storage. 44 (2021) 103439. https://doi.org/10.1016/j.est.2021.103439.

[24] F. von Bülow, T. Meisen, State of Health Forecasting of Heterogeneous Lithium-ion Battery Types and Operation Enabled by Transfer Learning, PHM Society European Conference. 7 (2022) 490–508. https://doi.org/10.36001/phme.2022.v7i1.3312.

[25] P. Keil, Aging of Lithium-Ion Batteries in Electric Vehicles. PhD Thesis. Technische Universität München (TUM), München, Germany, 2017. https://mediatum.ub.tum.de/doc/1355829/file.pdf.

[26] M.-T. von Srbik, Advanced lithium-ion battery modelling for automotive applications. PhD Thesis. Imperial College London, London, UK, 2015.

[27] H. Dahn, G.M. Ehrlich, Lithium-Ion Batteries, in: T.B. Reddy, D. Linden (Eds.), Linden's handbook of batteries, McGraw-Hill, New York, NY, US, 2011, 26.1-26.80.

[28] K. Vuorilehto, Materials and function, in: R. Korthauer (Ed.), Lithium-Ion Batteries: Basics and Applications, Springer Berlin Heidelberg, Berlin, Heidelberg, Germany, 2018, pp. 21–28.

[29] W. Waag, C. Fleischer, D.U. Sauer, Critical review of the methods for monitoring of lithium-ion batteries in electric and hybrid vehicles, J. of Power Sources. 258 (2014) 321–339. https://doi.org/10.1016/j.jpowsour.2014.02.064.

[30] L. Chen, Z. Lü, W. Lin, J. Li, H. Pan, A new state-of-health estimation method for lithium-ion batteries through the intrinsic relationship between ohmic internal resistance and capacity, Meausrement. 116 (2018) 586–595. https://doi.org/10.1016/j.measurement.2017.11.016.

[31] M.S.H. Lipu, M.A. Hannan, A. Hussain, M.M. Hoque, P.J. Ker, M.H.M. Saad, A. Ayob, A review of state of health and remaining useful life estimation methods for lithium-ion battery in electric vehicles, Journal of Cleaner Production. 205 (2018) 115–133. https://doi.org/10.1016/j.jclepro.2018.09.065.

[32] W. Diao, J. Jiang, C. Zhang, H. Liang, M.G. Pecht, Energy state of health estimation for battery packs based on the degradation and inconsistency, Energy Procedia. 142 (2017) 3578–3583. https://doi.org/10.1016/j.egypro.2017.12.248.

[33] H. He, Y. Zhang, R. Xiong, C. Wang, A novel Gaussian model based battery state estimation approach, Applied Energy. 151 (2015) 41–48. https://doi.org/10.1016/j.apenergy.2015.04.062.

[34] A. Kirchev, Battery Management and Battery Diagnostics, in: J. Garche, P.T. Moseley, P. Adelmann (Eds.), Electrochemical energy storage for renewable sources and grid balancing, Elsevier, Amsterdam, The Netherlands, 2015, pp. 411–435.

[35] Y. Zhang, R. Xiong, H. He, W. Shen, Lithium-Ion Battery Pack State of Charge and State of Energy Estimation Algorithms Using a Hardware-in-the-Loop Validation, IEEE Trans. Power Electron. 32 (2017) 4421–4431. https://doi.org/10.1109/TPEL.2016.2603229.

[36] Bundesministeriums der Justiz, Verordnung über Verbraucherinformationen zu Kraftstoffverbrauch, CO_2-Emissionen und Stromverbrauch neuer Personenkraftwagen (Pkw-Energieverbrauchskennzeichnungsverordnung), 2004.

[37] T. Tanaka, S. Ito, M. Muramatsu, T. Yamada, H. Kamiko, N. Kakimoto, Y. Inui, Accurate and versatile simulation of transient voltage profile of lithium-ion secondary battery employing internal equivalent electric circuit, Applied Energy. 143 (2015) 200–210. https://doi.org/10.1016/j.apenergy.2015.01.028.

[38] United Nations Economic Commission for Europe (UNECE), Addendum 22: United Nations Global Technical Regulation (GTR) No. 22. https://unece.org/sites/default/files/2022-04/ECE_TRANS_180a22e.pdf, 2022 (accessed 1.03.2023).

[39] United Nations Economic Commission for Europe (UNECE), Major auto markets join forces for draft UN legislation on electric vehicle battery durability. https://unece.org/media/press/362038, 2021 (accessed 1.03.2023).

[40] United Nations Economic Commission for Europe (UNECE), UBE Provides Battery Durability Insight. https://wiki.unece.org/download/attachments/109351800/EVE-38-06e.pdf, 2020 (accessed 1.03.2023).

[41] L. Calearo, C. Ziras, A. Thingvad, M. Marinelli, Agnostic Battery Management System Capacity Estimation for Electric Vehicles, Energies. 15 (2022) 9656. https://doi.org/10.3390/en15249656.

[42] T. Gewald, A. Candussio, L. Wildfeuer, D. Lehmkuhl, A. Hahn, M. Lienkamp, Accelerated aging characterization of lithium-ion cells, Batteries. 6 (2020) 6. https://doi.org/10.3390/batteries6010006.

[43] B.P. Matadi, S. Geniès, A. Delaille, T. Waldmann, M. Kasper, M. Wohlfahrt-Mehrens, F. Aguesse, E. Bekaert, I. Jiménez-Gordon, L. Daniel, X. Fleury, M. Bardet, J.-F. Martin, Y. Bultel, Effects of biphenyl polymerization on lithium deposition in commercial graphite/NMC lithium-ion pouch-cells during calendar aging at high temperature, J. Electrochem. Soc. 164 (2017) A1089-A1097. https://doi.org/10.1149/2.0631706jes.

[44] J. Jaguemont, L. Boulon, Y. Dubé, A comprehensive review of lithium-ion batteries used in hybrid and electric vehicles at cold temperatures, Appl. Energy. 164 (2016) 99–114. https://doi.org/10.1016/j.apenergy.2015.11.034.

[45] A. Barré, B. Deguilhem, S. Grolleau, M. Gérard, F. Suard, D. Riu, A review on lithium-ion battery ageing mechanisms and estimations for automotive applications, J. of Power Sources. 241 (2013) 680–689. https://doi.org/10.1016/j.jpowsour.2013.05.040.

[46] A. Marongiu, M. Roscher, D.U. Sauer, Influence of the vehicle-to-grid strategy on the aging behavior of lithium battery electric vehicles, Appl. Energy. 137 (2015) 899–912. https://doi.org/10.1016/j.apenergy.2014.06.063.

[47] C. Birkl, Diagnosis and Prognosis of Degradation in Lithium-Ion Batteries. PhD Thesis. University of Oxford, Oxford, UK, 2017. https://ora.ox.ac.uk/objects/uuid:7d8ccb9c-1469-4209-9995-5871fc908b54/files/m0f85ce4df327a1b2604cdd066d4110c9 (accessed 1.03.2023).

[48] T.T. Nguyen, Big Data Alterungsanalyse von Fahrzeugantriebsbatterien zur Klassifizierung für stationäre Anwendungen. PhD Thesis. Technische Universität München (TUM), München, Germany, 2019. https://mediatum.ub.tum.de/doc/1488578/1488578.pdf (accessed 1.03.2023).

[49] P.M. Attia, A. Bills, F. Brosa Planella, P.A. Dechent, G. dos Reis, M. Dubarry, P. Gasper, R. Gilchrist, S. Greenbank, D.A. Howey, O. Liu, E. Khoo, Y. Preger, A. Soni, S. Sripad, A.G. Stefanopoulou, V. Sulzer, Review—"Knees" in Lithium-Ion Battery Aging Trajectories, J. Electrochem. Soc. 169 (2022) 60517. https://doi.org/10.1149/1945-7111/ac6d13.

[50] P. Fermín-Cueto, E. McTurk, M. Allerhand, E. Medina-Lopez, M.F. Anjos, J. Sylvester, G. dos Reis, Identification and machine learning prediction of knee-point and knee-onset in capacity degradation curves of lithium-ion cells, Energy and AI. 1 (2020) 100006. https://doi.org/10.1016/j.egyai.2020.100006.

[51] Y. Li, K. Liu, A.M. Foley, A. Zulke, M. Berecibar, E. Nanini-Maury, J. van Mierlo, H.E. Hoster, Data-driven health estimation and lifetime prediction of lithium-ion batteries: A review, Renewable and Sustain. Energy Rev. 113 (2019). https://doi.org/10.1016/j.rser.2019.109254.

[52] H. Sadegh Kouhestani, X. Yi, G. Qi, X. Liu, R. Wang, Y. Gao, X. Yu, L. Liu, Prognosis and Health Management (PHM) of Solid-State Batteries, Energies. 15 (2022) 6599. https://doi.org/10.3390/en15186599.

[53] K. Liu, Z. Wei, C. Zhang, Y. Shang, R. Teodorescu, Q.-L. Han, Towards Long Lifetime Battery, IEEE/CAA J. Autom. Sinica. 9 (2022) 1139–1165. https://doi.org/10.1109/JAS.2022.105599.

[54] T. Lombardo, M. Duquesnoy, H. El-Bouysidy, F. Årén, A. Gallo-Bueno, P.B. Jørgensen, A. Bhowmik, A. Demortière, E. Ayerbe, F. Alcaide, M. Reynaud, J. Carrasco, A. Grimaud, C. Zhang, T. Vegge, P. Johansson, A.A. Franco, Artificial Intelligence Applied to Battery Research, Chem. Rev. 122 (2022) 10899–10969. https://doi.org/10.1021/acs.chemrev.1c00108.

[55] International Organization for Standardization (ISO), Secondary cells and batteries containing alkaline or other non-acid electrolytes – Secondary lithium cells and batteries for use in industrial applications, 2014.

[56] A. Väyrynen, J. Salminen, Lithium ion battery production, The Journal of Chemical Thermodynamics. 46 (2012) 80–85. https://doi.org/10.1016/j.jct.2011.09.005.

[57] H. Wang, S. Wang, X. Feng, X. Zhang, K. Dai, J. Sheng, Z. Zhao, Z. Du, Z. Zhang, K. Shen, C. Xu, Q. Wang, X. Sun, Y. Li, J. Ling, J. Feng, H. Wang, M. Ouyang, An experimental study on the thermal characteristics of the Cell-To-Pack system, Energy. 227 (2021) 120338. https://doi.org/10.1016/j.energy.2021.120338.

[58] A. Kwade, W. Haselrieder, R. Leithoff, A. Modlinger, F. Dietrich, K. Droeder, Current status and challenges for automotive battery production technologies, Nat. Energy. 3 (2018) 290–300. https://doi.org/10.1038/s41560-018-0130-3.

[59] A. Kampker, Elektromobilproduktion, Springer Berlin Heidelberg, Berlin, Heidelberg, Germany, 2014.

[60] H. Löbberding, S. Wessel, C. Offermanns, M. Kehrer, J. Rother, H. Heimes, A. Kampker, From Cell to Battery System in BEVs, WEVJ. 11 (2020) 77. https://doi.org/10.3390/wevj11040077.

[61] A. Hauser, R.M. Kuhn, High-voltage battery management systems (BMS) for electric vehicles, in: B. Scrosati, J. Garche, W. Tillmetz (Eds.), Advances in battery technologies for electric vehicles, Woodhead Publishing, Cambridge, UK, 2015, pp. 265–282.

[62] A. Jossen, V. Späth, H. Döring, J. Garche, Reliable battery operation — a challenge for the battery management system, J. of Power Sources. 84 (1999) 283–286. https://doi.org/10.1016/S0378-7753(99)00329-8.

[63] Y. Hua, A.C. Cordoba-Arenas, N. Warner, G. Rizzoni, A multi time-scale state-of-charge and state-of-health estimation framework using nonlinear predictive filter for lithium-ion battery pack

with passive balance control, J. of Power Sources. 280 (2015) 293–312. https://doi.org/10.1016/j.jpowsour.2015.01.112.

[64] A.C. Cordoba-Arenas, S. Onori, G. Rizzoni, A control-oriented lithium-ion battery pack model for plug-in hybrid electric vehicle cycle-life studies and system design with consideration of health management, J. of Power Sources. 279 (2015) 791–808. https://doi.org/10.1016/j.jpowsour.2014.12.048.

[65] A. Mäki, S. Valkealahti, Power Losses in Long String and Parallel-Connected Short Strings of Series-Connected Silicon-Based Photovoltaic Modules Due to Partial Shading Conditions, IEEE Trans. Energy Convers. 27 (2012) 173–183. https://doi.org/10.1109/TEC.2011.2175928.

[66] J. McDowall, BATTERIES | Parallel and Series Connections, in: J. Garche (Ed.), Encyclopedia of electrochemical power sources, Elsevier, Amsterdam, The Netherlands, 2009, pp. 499–509.

[67] F. Feng, X. Hu, L. Hu, F. Hu, Y. Li, L. Zhang, Propagation mechanisms and diagnosis of parameter inconsistency within Li-Ion battery packs, Renewable and Sustain. Energy Rev. 112 (2019) 102–113. https://doi.org/10.1016/j.rser.2019.05.042.

[68] G.L. Plett, M.J. Klein, Simulating Battery Packs Comprising Parallel Cell Modules and Series Cell Modules, in: 24th International Battery, Hybrid and Fuel Cell Electric Vehicle Symposium & Exhibition (EVS 24), 2009, pp. 1–17.

[69] C. Luan, C. Ma, C. Wang, L. Chang, L. Xiao, Z. Yu, H. Li, Influence of the connection topology on the performance of lithium-ion battery pack under cell-to-cell parameters variations, J. of Energy Storage. 41 (2021) 102896. https://doi.org/10.1016/j.est.2021.102896.

[70] C.-Y. Chang, P. Tulpule, G. Rizzoni, W. Zhang, X. Du, A probabilistic approach for prognosis of battery pack aging, J. of Power Sources. 347 (2017) 57–68. https://doi.org/10.1016/j.jpowsour.2017.01.130.

[71] X. Wang, Z. Wang, L. Wang, Z. Wang, H. Guo, Dependency analysis and degradation process-dependent modeling of lithium-ion battery packs, J. of Power Sources. 414 (2019) 318–326. https://doi.org/10.1016/j.jpowsour.2019.01.021.

[72] S.F. Schuster, M.J. Brand, P. Berg, M. Gleissenberger, A. Jossen, Lithium-ion cell-to-cell variation during battery electric vehicle operation, J. of Power Sources. 297 (2015) 242–251. https://doi.org/10.1016/j.jpowsour.2015.08.001.

[73] M. Dubarry, G. Baure, C. Pastor-Fernandez, T.F. Yu, W.D. Widanage, J. Marco, Battery energy storage system modeling: A combined comprehensive approach, J. of Energy Storage. 21 (2019) 172–185. https://doi.org/10.1016/j.est.2018.11.012.

[74] T. Bruen, J. Marco, Modelling and experimental evaluation of parallel connected lithium ion cells for an electric vehicle battery system, J. of Power Sources. 310 (2016) 91–101. https://doi.org/10.1016/j.jpowsour.2016.01.001.

[75] D.H. Jung, D.M. Kim, J. Park, S.-i. Kim, T. Kim, Cycle-life prediction model of lithium iron phosphate-based lithium-ion battery module, Int. J. Energy Res. 45 (2021) 16489–16496. https://doi.org/10.1002/er.6895.

[76] S.-L. Jeng, C.M. Tan, P.-C. Chen, Statistical distribution of Lithium-ion batteries useful life and its application for battery pack reliability, J. of Energy Storage. 51 (2022) 104399. https://doi.org/10.1016/j.est.2022.104399.

[77] C. Pastor-Fernandez, T. Bruen, W.D. Widanage, M.A. Gama-Valdez, J. Marco, A Study of Cell-to-Cell Interactions and Degradation in Parallel Strings, J. of Power Sources. 329 (2016) 574–585. https://doi.org/10.1016/j.jpowsour.2016.07.121.

[78] M. Dubarry, D.A.C. Beck, Perspective on Mechanistic Modeling of Li-Ion Batteries, Acc. Mater. Res. 3 (2022) 843–853. https://doi.org/10.1021/accountsmr.2c00082.

[79] M.P. Naylor Marlow, Understanding the effects of heterogeneities on battery pack lifetime. PhD Thesis. Imperial College London, London, UK, 2021.

[80] S. Petrovic, Battery Technology Crash Course, 1st ed., Springer International Publishing, Cham, Switzerland, 2021.

[81] B. Saha, K. Goebel, Battery Data Set. https://www.nasa.gov/content/prognostics-center-of-excellence-data-set-repository, 2008 (accessed 1.03.2023).

[82] D.U. Sauer, Time-series cyclic aging data on 48 commercial NMC/ graphite Sanyo/ Panasonic UR18650E cylindrical cells, 2021 (accessed 1.03.2023).

[83] T. Raj, A.A. Wang, C.W. Monroe, D.A. Howey, Investigation of Path‑Dependent Degradation in Lithium - Ion Batteries, Batteries & Supercaps. 3 (2020) 1377 – 1385. https://doi.org/10.1002/batt.202000160.

[84] P.M. Attia, A. Grover, N. Jin, K.A. Severson, T.M. Markov, Y.-H. Liao, M.H. Chen, B. Cheong, N. Perkins, Z. Yang, P.K. Herring, M. Aykol, S.J. Harris, R.D. Braatz, S. Ermon, W.C. Chueh, Closed-loop optimization of fast-charging protocols for batteries with machine learning, Nature. 578 (2020) 397–402. https://doi.org/10.1038/s41586-020-1994-5.

[85] K.A. Severson, P.M. Attia, N. Jin, N. Perkins, B. Jiang, Z. Yang, M.H. Chen, M. Aykol, P.K. Herring, D. Fraggedakis, M.Z. Bazant, S.J. Harris, W.C. Chueh, R.D. Braatz, Data-driven prediction of battery cycle life before capacity degradation, Nat. Energy. 4 (2019) 383–391. https://doi.org/10.1038/s41560-019-0356-8.

[86] G. Baure, M. Dubarry, Synthetic vs. Real Driving Cycles, Batteries. 5 (2019) 42. https://doi.org/10.3390/batteries5020042.

[87] A. Nuhic, T. Terzimehic, T. Soczka-Guth, M. Buchholz, K. Dietmayer, Health diagnosis and remaining useful life prognostics of lithium-ion batteries using data-driven methods, J. of Power Sources. 239 (2013) 680–688. https://doi.org/10.1016/j.jpowsour.2012.11.146.

[88] D.-I. Stroe, M.J. Swierczynski, S. Knudesn Kær, E. Martinez-Laserna, E. Sarasketa-Zabala, Accelerated aging of Lithium-ion batteries based on electric vehicle mission profile, in: ECCE 2017, IEEE, Piscataway, NJ, US, 2017.

[89] M.S. Hosen, J. Jaguemont, J. van Mierlo, M. Berecibar, Battery lifetime prediction and performance assessment of different modeling approaches, iScience. 24 (2021). https://doi.org/10.1016/j.isci.2021.102060.

[90] S. Micari, S. Foti, A. Testa, S. de Caro, F. Sergi, L. Andaloro, D. Aloisio, G. Napoli, Reliability assessment and lifetime prediction of Li-ion batteries for electric vehicles, Electr. Eng. 104 (2022) 165–177. https://doi.org/10.1007/s00202-021-01288-4.

[91] G. Pozzato, A. Allam, S. Onori, Lithium-ion battery aging dataset based on electric vehicle real-driving profiles, Data in brief. 41 (2022) 107995. https://doi.org/10.1016/j.dib.2022.107995.

[92] J. Stadler, C. Krupp, M. Ecker, J. Bandlow, B. Spier, A. Latz, Investigation and modeling of cyclic aging using a design of experiment with automotive grade lithium-ion cells, J. of Power Sources. 521 (2022) 230952. https://doi.org/10.1016/j.jpowsour.2021.230952.

[93] L. von Kolzenberg, J. Stadler, J. Fath, M. Ecker, B. Horstmann, A. Latz, A four parameter model for the solid-electrolyte interphase to predict battery aging during operation, J. of Power Sources. 539 (2022). https://doi.org/10.1016/j.jpowsour.2022.231560.

[94] J. Schmitt, M. Rehm, A. Karger, A. Jossen, Aging data, charging curves and battery electric vehicle application profiles of a nickel-rich NMC / silicon-graphite high-energy lithium-ion cell, 2023.

[95] A. Barré, F. Suard, M. Gérard, M. Montaru, D. Riu, Statistical analysis for understanding and predicting battery degradations in real-life electric vehicle use, J. of Power Sources. 245 (2014) 846–856. https://doi.org/10.1016/j.jpowsour.2013.07.052.

[96] B. Bole, C.S. Kulkarni, M. Daigle, Randomized Battery Usage Data Set. https://www.nasa.gov/content/prognostics-center-of-excellence-data-set-repository, 2012 (accessed 1.03.2023).

[97] P. Jones, U. Stimming, A. Lee, Impedance-based forecasting of battery performance amid uneven usage, 2021 (accessed 1.03.2023).

[98] M. Huotari, S. Arora, A. Malhi, K. Främling, A Dynamic Battery State-of-Health Forecasting Model for Electric Trucks, in: Volume 8: Energy, American Society of Mechanical Engineers, 2020.

[99] M. Simão, R. Prytz, S. Nowaczyk, Long-term Evaluation of the State-of-Health of Traction Lithium-ion Batteries in Operational Buses, IJPHM. 13 (2022). https://doi.org/10.36001/ijphm.2022.v13i1.3115.

[100] I. Semanjski, S. Gautama, Forecasting the State of Health of Electric Vehicle Batteries to Evaluate the Viability of Car Sharing Practices, Energies. 9 (2016) 1025. https://doi.org/10.3390/en9121025.

[101]   F. Yao, D. Meng, Y. Wu, Y. Wan, F. Ding, Online health estimation strategy with transfer learning for operating lithium-ion batteries, J. Power Electron. 239 (2023) 1526. https://doi.org/10.1007/s43236-023-00605-3.

[102]   A. Tomaszewska, Z. Chu, X. Feng, S. O'Kane, X. Liu, J. Chen, C. Ji, E. Endler, R. Li, L. Liu, Y. Li, S. Zheng, S. Vetterlein, M. Gao, J. Du, M. Parkes, M. Ouyang, M. Marinescu, G.J. Offer, B. Wu, Lithium-ion battery fast charging, eTransportation. 1 (2019) 100011. https://doi.org/10.1016/j.etran.2019.100011.

[103]   B. Bole, C.S. Kulkarni, M. Daigle, Adaptation of an Electrochemistry-based Li-Ion Battery Model to Account for Deterioration Observed Under Randomized Use, in: Annual Conference of the Prognostics and Health Management Society, 2012.

[104]   United Nations Economic Commission for Europe (UNECE), Addendum 15: Global technical regulation (GTR) No. 15. https://unece.org/fileadmin/DAM/trans/main/wp29/wp29wgs/wp29gen/wp29registry/ECE-TRANS-180a15am5e.pdf, 2019 (accessed 1.03.2023).

[105]   United States Environmental Protection Agency (US EPA), Dynamometer Drive Schedules. https://www.epa.gov/vehicle-and-fuel-emissions-testing/dynamometer-drive-schedules#UDDS, 2021 (accessed 1.03.2023).

[106]   F.K.-D. Noering, Unsupervised Pattern Discovery in Automotive Time Series, 1st ed., Springer Fachmedien Wiesbaden, Wiesbaden, Germany, 2022.

[107]   G. Steinbuß, B. Rzepka, S. Bischof, T. Blank, K. Böhm, FOBSS: Monitoring Data from a Modular Battery System, in: e-Energy '19: Proceedings of the Tenth ACM International Conference on Future Energy Systems, Association for Computing Machinery Inc. (ACM), New York, NY, US, 2019, pp. 456–459.

[108]   K. de Craemer, K. Trad, Cyclic ageing with driving profile of a lithium ion battery module, 2021 (accessed 1.03.2023).

[109]   W. He, N. Williard, M. Osterman, M.G. Pecht, Prognostics of lithium-ion batteries based on Dempster–Shafer theory and the Bayesian Monte Carlo method, J. of Power Sources. 196 (2011) 10314–10321. https://doi.org/10.1016/j.jpowsour.2011.08.040.

[110]   S. Saxena, Y. Xing, M.G. Pecht, PHM of Li-ion Batteries, in: M.G. Pecht, M. Kang (Eds.), Prognostics and Health Management of Electronics, John Wiley and Sons Ltd, Chichester, UK, 2018, pp. 349–375.

[111]   M. Amer, T.U. Daim, A. Jetter, A review of scenario planning, Futures. 46 (2013) 23–40. https://doi.org/10.1016/j.futures.2012.10.003.

[112]   U. Pillkahn, Using Trends and Scenarios as Tools for Strategy Development, 1st ed., Wiley-VCH, Hoboken, NJ, US, 2008.

[113]   M.E. Porter, Competitive advantage, 1st ed., Free Press, New York, NY, US, 1998.

[114]   F. von Bülow, F. Heinrich, T. Meisen, Fleet Management Approach for Manufacturers displayed at the Use Case of Battery Electric Vehicles, in: IEEE International Conference on Systems, Man, and Cybernetics (SMC), IEEE, 2021, pp. 3218–3225.

[115]   J.G. de Gooijer, R.J. Hyndman, 25 years of time series forecasting, Int. J. of Forecasting. 22 (2006) 443–473. https://doi.org/10.1016/j.ijforecast.2006.01.001.

[116]   J.S. Pruitt, T. Adlin, The persona lifecycle, Elsevier, Amsterdam, Boston, 2006.

[117]   A. Cooper, The inmates are running the asylum, 6th ed., Sams, Indianapolis, IN, US, 2006.

[118]   S. Zhao, C. Zhang, Y. Wang, Lithium-ion battery capacity and remaining useful life prediction using board learning system and long short-term memory neural network, J. of Energy Storage. 52 (2022) 104901. https://doi.org/10.1016/j.est.2022.104901.

[119]   L. Yao, S. Xu, A. Tang, F. Zhou, J. Hou, Y. Xiao, Z. Fu, A Review of Lithium-Ion Battery State of Health Estimation and Prediction Methods, WEVJ. 12 (2021) 113. https://doi.org/10.3390/wevj12030113.

[120]   H. Tian, P. Qin, K. Li, Z. Zhao, Review and recent advances in battery health monitoring and prognostics technologies for electric vehicle (EV) safety and mobility, Journal of Cleaner Production. 261 (2020). https://doi.org/10.1016/j.jclepro.2020.120813.

[121]   S.M. Rezvanizaniani, Z. Liu, Y. Chen, J. Lee, Review and recent advances in battery health monitoring and prognostics technologies for electric vehicle (EV) safety and mobility, J. of Power Sources. 256 (2014) 110–124. https://doi.org/10.1016/j.jpowsour.2014.01.085.

[122] J. Schijve, Load Spectra, in: J. Schijve (Ed.), Fatigue of Structures and Materials, Springer Netherlands, Dordrecht, The Netherlands, 2009, pp. 259–293.

[123] C. Sugihara, K. Sutton, A. Davis, V. Karanam, G. Tal, From sport to eco, Transp. Res. Part F: Traffic Psychol. and Behav. 82 (2021) 412–428. https://doi.org/10.1016/j.trf.2021.09.007.

[124] F. von Bülow, F. Heinrich, T. Meisen, A new perspective for manufacturers: Cloud-based utilization of operational fleet data, in: VDI Wissensforum GmbH (Ed.), ELIV 2021, VDI Verlag, Düsseldorf, Germany, 2021, pp. 117–130.

[125] R.R. Richardson, M.A. Osborne, D.A. Howey, Gaussian process regression for forecasting battery state of health, J. of Power Sources. 357 (2017) 209–219. https://doi.org/10.1016/j.jpowsour.2017.05.004.

[126] X. Tang, K. Liu, X. Wang, F. Gao, J. Macro, W.D. Widanage, Model Migration Neural Network for Predicting Battery Aging Trajectories, IEEE Trans. Transport. Electrific. 6 (2020) 363–374. https://doi.org/10.1109/TTE.2020.2979547.

[127] J. Guo, Z.J. Li, M.G. Pecht, A Bayesian approach for Li-Ion battery capacity fade modeling and cycles to failure prognostics, J. of Power Sources. 281 (2015) 173–184. https://doi.org/10.1016/j.jpowsour.2015.01.164.

[128] L. Song, K. Zhang, T. Liang, X. Han, Y. Zhang, Intelligent state of health estimation for lithium-ion battery pack based on big data analysis, J. of Energy Storage. 32 (2020) 101836. https://doi.org/10.1016/j.est.2020.101836.

[129] J. Li, Z. Deng, H. Liu, Y. Xie, C. Liu, C. Lu, Battery capacity trajectory prediction by capturing the correlation between different vehicles, Energy. 260 (2022) 125123. https://doi.org/10.1016/j.energy.2022.125123.

[130] S. Rohr, S. Müller, M. Baumann, M. Kerler, F. Ebert, D. Kaden, M. Lienkamp, Quantifying Uncertainties in Reusing Lithium-Ion Batteries from Electric Vehicles, Procedia Manufacturing. 8 (2017) 603–610. https://doi.org/10.1016/j.promfg.2017.02.077.

[131] D. Andre, C. Appel, T. Soczka-Guth, D.U. Sauer, Advanced mathematical methods of SOC and SOH estimation for lithium-ion batteries, J. of Power Sources. 224 (2013) 20–27. https://doi.org/10.1016/j.jpowsour.2012.10.001.

[132]   Y. Zhang, T. Wik, J. Bergström, M.G. Pecht, C. Zou, A machine learning-based framework for online prediction of battery ageing trajectory and lifetime using histogram data, J. of Power Sources. 526 (2022) 231110. https://doi.org/10.1016/j.jpowsour.2022.231110.

[133]   N. Hartmann, E.D. Özdemir, Impact of different utilization scenarios of electric vehicles on the German grid in 2030, J. of Power Sources. 196 (2011) 2311–2318. https://doi.org/10.1016/j.jpowsour.2010.09.117.

[134]   B. Tepe, J. Figgener, S. Englberger, D.U. Sauer, A. Jossen, H. Hesse, Optimal pool composition of commercial electric vehicles in V2G fleet operation of various electricity markets, Appl. Energy. 308 (2022) 118351. https://doi.org/10.1016/j.apenergy.2021.118351.

[135]   C. Nobis, T. Kuhnimhof, Mobilität in Deutschland – MiD. Ergebnisbericht. https://elib.dlr.de/125879/1/MiD2017_Ergebnisbericht.pdf, 2018 (accessed 1.03.2023).

[136]   M.N. Mladenović, Mobility as a Service, in: R. Vickerman (Ed.), International Encyclopedia of Transportation, Elsevier, San Diego, CA, US, 2021, pp. 12–18.

[137]   S. Greenbank, D.A. Howey, Automated Feature Extraction and Selection for Data-Driven Models of Rapid Battery Capacity Fade and End of Life, IEEE Trans. Ind. Inf. 18 (2022) 2965–2973. https://doi.org/10.1109/TII.2021.3106593.

[138]   S. Bamati, H. Chaoui, Lithium-Ion Batteries Long Horizon Health Prognostic Using Machine Learning, IEEE Trans. Energy Convers. 37 (2022) 1176–1186. https://doi.org/10.1109/TEC.2021.3111525.

[139]   P.K. Jones, U. Stimming, A.A. Lee, Impedance-based forecasting of lithium-ion battery performance amid uneven usage, Nature Communications. 13 (2022). https://doi.org/10.1038/s41467-022-32422-w.

[140]   A. Perez, F. Jaramillo, V. Quintero, M.E. Orchard, Characterizing the degradation process of Lithium-Ion Batteries using a Similarity-Based-Modeling Approach, Fourth European Conference of the Prognostics and Health Management Society 2018 (2019). https://doi.org/10.36001/phme.2018.v4i1.439.

[141]   K. Liu, X. Hu, Z.B. Wei, Y. Li, Y. Jiang, Modified Gaussian Process Regression Models for Cyclic Capacity Prediction of Lithium-Ion Batteries, IEEE Trans. Transport. Electrific. 5 (2019) 1225–1236. https://doi.org/10.1109/TTE.2019.2944802.

[142]   F. von Bülow, Y. Hahn, R. Meyes, T. Meisen, Transparent and Interpretable State of Health Forecasting of Lithium-ion Batteries with Deep Learning and Saliency Maps, Int. J. Energy Res. Under Review (2023).

[143]   J.S. Bergstra, R. Bardenet, Y. Bengio, B. Kégl, Algorithms for Hyper-Parameter Optimization, in: J. Shawe-Taylor, R. Zemel, P. Bartlett, F. Pereira, K.Q. Weinberger (Eds.), 25th Annual Conference on Neural Information Processing Systems 2011, Curran Associates Inc., 2011, pp. 2546–2554.

[144]   J.S. Bergstra, D. Yamins, D. Cox, Making a science of model search: hyperparameter optimization in hundreds of dimensions for vision architecture, in: S. Dasgupta, D. McAllester (Eds.), Proceedings of the 30th International Conference on Machine Learning, PMLR, 2013, pp. 115–123.

[145]   C.M. Bishop, Pattern recognition and machine learning, 8th ed., Springer, New York, NY, US, 2009.

[146]   P. Keil, S.F. Schuster, J. Wilhelm, J. Travi, A. Hauser, R.C. Karl, A. Jossen, Calendar Aging of Lithium-Ion Batteries, J. Electrochem. Soc. 163 (2016) A1872-A1880. https://doi.org/10.1149/2.0411609jes.

[147]   D.-I. Stroe, Lifetime Models for Lithium-ion Batteries used in Virtual Power Plant Applications. PhD Thesis. Aalborg University, Aalborg, Denmark, 2014. https://vbn.aau.dk/da/publications/d56e6622-f1bd-4a88-b82f-f42e6a81e86a.

[148]   G. Baure, A. Devie, M. Dubarry, Battery Durability and Reliability under Electric Utility Grid Operations, J. Electrochem. Soc. 166 (2019) A1991-A2001. https://doi.org/10.1149/2.0971910jes.

[149]   S. Hahn, S. Theil, J. Kroggel, K.P. Birke, Pressure Prediction Modeling and Validation for Lithium-Ion Pouch Cells in Buffered Module Assemblies, J. of Energy Storage. 40 (2021). https://doi.org/10.1016/j.est.2021.102517.

[150] W. Li, Z. Jiao, Q. Xiao, J. Meng, Y. Mu, H. Jia, R. Teodorescu, F. Blaabjerg, A Study on Performance Characterization Considering Six-Degree-of-Freedom Vibration Stress and Aging Stress for Electric Vehicle Battery Under Driving Conditions, IEEE Access. 7 (2019) 112180–112190. https://doi.org/10.1109/ACCESS.2019.2935380.

[151] S.J. Pan, Q. Yang, A Survey on Transfer Learning, IEEE Trans. Knowl. Data Eng. 22 (2010) 1345–1359. https://doi.org/10.1109/TKDE.2009.191.

[152] N. Rasmekomen, A.K. Parlikad, Optimising Maintenance of Multi-Component Systems with Degradation Interactions, IFAC Proceedings Volumes. 47 (2014) 7098–7103. https://doi.org/10.3182/20140824-6-ZA-1003.01447.

[153] P. Do, R. Assaf, P. Scarf, B. Iung, Modelling and application of condition-based maintenance for a two-component system with stochastic and economic dependencies, Reliability Engineering and System Safety. 182 (2019) 86–97. https://doi.org/10.1016/j.ress.2018.10.007.

[154] V.-T. Nguyen, P. Do, A. Voisin, Artificial-Intelligence-Based Maintenance Scheduling for Complex Systems with Multiple Dependencies, PHM Society European Conference. 7 (2022) 586–589. https://doi.org/10.36001/phme.2022.v7i1.3294.

[155] P. Chanchaipo, L. Sirikul, EV battery degradation forecasting based on high dimensional data. Master Thesis. Chalmers University of Technology, Göteborg, Sweden, 2020. https://hdl.handle.net/20.500.12380/302222.

[156] A. Aitio, D.A. Howey, Combining Non-Parametric and Parametric Models for Stable and Computationally Efficient Battery Health Estimation, in: Proceedings of the ASME 2020 Dynamic Systems and Control Conference (DSCC2020), Volume 1, The American Society of Mechanical Engineers, New York, NY, US, 2020.

[157] E. Frisk, M. Krysander, E. Larsson, Data-Driven Lead-Acid Battery Prognostics Using Random Survival Forests, Annu. Conf. of the Prognostics and Health Manage. Soc. 6 (2014). https://doi.org/10.36001/phmconf.2014.v6i1.2370.

[158] Volkswagen AG, Key components for a new era – the battery system. https://www.volkswagenag.com/en/news/2019/12/key-components-for-a-new-era--the-battery-system.html, 2019 (accessed 1.03.2023).

Appendix

Battery Pack Data in Literature Review

Table 12: Overview of data sets of papers apparent in our literature review [12]. Only data sets of batteries on pack level are listed. All other data sets are on battery-cell level. Specification of the operational context following Table 4.

Source	Vehicle type	Amount of batteries	Operational context	Battery type
[100]	EV	2	Car-sharing service	Lithium-ion
[155]	PHEV	7,247	Private owners	Lithium-ion (NMC)
[95]	EV	1	Driver following predefined profile (I-VC.3) and parts of test bench	Lithium-ion (LFP)
[90]	Pack composed of 85 cells	1	Representative driving profile (I-VC.2)	Lithium-ion (NMC)
[156]	Pack composed of 6 cells in series	1,027	Connected to photovoltaic (PV) system	Lead-acid
[157]	Heavy-duty trucks	33,603	LV starter battery	Lead-acid

Definitions of Battery Pack and Battery System

Table 13: Overview of different definitions of the terms battery module, battery pack, and battery system. "x" means required. "-" means not required. "Opt." means optional component.

Source	Definition of			Components						
	Module	Pack	System	Cells	Modules	Packs	Housing	Cooling system	BMS	Peripherals
[56]	x			x	-	-	x	x	Slave	x
[56]		x		-	x	x	-	x	-	x
[56]			x	-	-	x	-	x	Master	x
[55]	x			x	-	-	-	-	Opt.	-
[55]		x		x	x	-	Opt.	Opt.	Opt.	Opt.
[58]	x			x	-	-	x	-	x[20]	x[20]
[58]		x		-	x	-	x	Opt.	x	wiring
[59]	x			x	-	-	-	-	-	-
[59]		x		x	-	-	x	As function of housing	x	-
[59]			x		x	-	-	-	-	DC/DC converter
[61]	x			x	-	-	-	-	-	-
[61]		x		-	x[21]	-	-	-	-	-
[60]			x	-	x	-	x	-[22]	x	Sensor and controllers
[158]			x	-	x	-	-	-	-	-

Derivation of SOH Signal Discretization Error

Based on the relative discretization error ε_E of the measured energy signal E_measured from the true energy signal E_true:

$$E_\text{measured} = E_\text{true} \cdot (1 + \varepsilon_\text{E}) \Leftrightarrow \varepsilon_\text{E} = \frac{E_\text{measured} - E_\text{true}}{E_\text{true}} \tag{10}$$

we estimate the maximum relative discretization error ε_E of the energy signal:

$$\begin{aligned}\max(\varepsilon_\text{E}) &= \frac{\max(E_\text{measured} - E_\text{true})}{\min(E_\text{true})} = \frac{0.5 \cdot R_\text{E}}{\min(SOE) \cdot E_\text{max}} = \frac{0.5 \cdot R_\text{E}}{0.8 \cdot 0.8 \cdot E_\text{nom}} \\ &= \frac{0.5 \cdot 50\ Wh}{0.8 \cdot 0.8 \cdot 87\ kWh} = 0.000449\end{aligned} \tag{11}$$

assuming that the battery SOH is always determined at $SOE \geq 80\ \%$ and $SOH \geq 80\ \%$ because of the EOL with R_E as resolution of the energy signal.

Analogous to Eq. (11), we estimate the maximum relative discretization error ε_SOE of the SOE signal:

---

[20] „dedicated electronics for voltage, current and temperature control" [58]

[21] Self-reference of the terms pack and system: "[…] the term 'battery pack' or 'pack' is employed to describe a unit of multiple modules connected to form a HV battery system […]." [61]

[22] Only thermal management is listed which is seen as a function of the BMS in other literature.

$$\max(\varepsilon_{\text{SOE}}) = \frac{\max(SOE_{\text{measured}} - SOE_{\text{true}})}{\min(SOE_{\text{true}})} = \frac{0.5 \cdot R_{\text{SOE}}}{80\ \%} = \frac{0.5 \cdot 0.5\ \%}{80\ \%} = 0.3125 \tag{12}$$

with SOE_{measured} and SOE_{true} as measured and true SOE respectively and R_{SOE} as resolution of the SOE signal.

Analogous to Eq. (10), we define for the SOH:

$$SOH_{\text{measured}} = SOH_{\text{true}} \cdot (1 + \varepsilon_{\text{SOH}}). \tag{13}$$

From Eq. (7) follows for SOH_{measured}:

$$SOH_{\text{measured}} = \frac{E_{\text{measured}}}{SOE_{\text{measured}} \cdot E_{\text{nom}}} \tag{14}$$

with $E_{\text{nom}} = const$. Using Eq. (10) for E_{measured} and SOE_{measured} we obtain:

$$SOH_{\text{measured}} = \frac{E_{\text{true}} \cdot (1 + \varepsilon_{\text{E}})}{SOE_{\text{true}} \cdot (1 + \varepsilon_{\text{SOC}}) \cdot E_{\text{nom}}} = \frac{E_{\text{true}}}{SOE_{\text{true}} \cdot E_{\text{nom}}} \cdot \frac{1 + \varepsilon_E}{1 + \varepsilon_{SOE}} = SOH_{\text{true}} \cdot \frac{1 + \varepsilon_E}{1 + \varepsilon_{SOE}}. \tag{15}$$

With Eq. (13) and (15) we define:

$$1 + \varepsilon_{\text{SOH}} \coloneqq \frac{1 + \varepsilon_{\text{E}}}{1 + \varepsilon_{\text{SOE}}}. \tag{16}$$

and reformulate it as:

$$\varepsilon_{\text{SOH}} = \frac{1 + \varepsilon_{\text{E}}}{1 + \varepsilon_{\text{SOE}}} - 1 = \frac{\varepsilon_{\text{E}} - \varepsilon_{\text{SOE}}}{1 + \varepsilon_{\text{SOE}}}. \tag{17}$$

The maximum possible of ε_{SOH} in Eq. (17) is reached for maximum positive ε_{E} and maximum negative ε_{SOE}:

$$\varepsilon_{\text{SOH}} = \frac{\varepsilon_{\text{E}} - \varepsilon_{\text{SOE}}}{1 + \varepsilon_{\text{SOE}}} = \frac{0.000449 - (-0.3125)}{1 + (-0.3125)} = 0.0036 = 0.36\ \%. \tag{18}$$

Characteristics of best Models with Histogram-based Features

Table 14: Characteristics of best models with histogram-based features

Model No.	H1	H2	H3	H4
DOE parameters				
Window Width	10	25	50	100
Window Shift	5	10	25	25
Interval Resolution	coarse	coarse	coarse	coarse
Histogram Dimensions	2D	2D	2D	2D
Input Features	A	A	A	A
Data Characteristics				
No. of Features	369	369	369	369
No. of Samples	16,439	7,832	3,081	2,052
Hyperparameters				
Batch Size	128	128	128	32
Learning Rate	0.00025	0.00028	0.0002	0.0078
Regularization parameter (λ_1, λ_2)	(0, 0)	0	(0.0003, 0)	(0, 0.0014)
Dropout Rate	0.25	0.25	0	0
MLP Layout	[260, 360, 460, 460, 340, 140, 220]	[180, 380]	[380, 440, 260, 480, 80, 200, 260, 440, 60, 340, 100, 360, 80, 60, 360]	[80, 440, 240, 380, 340, 160, 220]
Model Complexity				
No. of Hidden Layers	7	2	15	7
No. of Model Parameter	804,001	135,761	943,681	482,401
Training time in s	1,096	171	1173	93

Characteristics of best Models with Accessible Features

Table 15: Characteristics of best models with accessible features

Model No.	SF1	SF2	SF3	SF4
DOE parameters				
Window Width	10	25	50	100
Window Shift	5	10	10	10
Input Features	3.1	3.1	3.1	3.1
Data Characteristics				
No. of Features	10	10	10	10
No. of Samples	16,439	7,832	3,081	2,052
Hyperparameters				
Batch Size	128	128	64	64
Learning Rate	0.00083	0.00023	0.00024	0.00057
Regularization parameter (λ_1, λ_2)	(0, 0)	(0.0002, 0)	(0, 0.0002)	(0.0001, 0)
Dropout Rate	0.24	0	0	0
MLP Layout	[260, 100, 60]	[260, 280, 420, 460, 380, 200, 280]	[420, 400, 480, 340, 200, 280, 160]	[400, 280, 460, 340, 380, 80]
Model Complexity				
No. of Hidden Layers	3	7	7	6
No. of Model Parameter	35,341	695,821	699,061	563,221
Training time in s	140	908	546	232

Comparison of Model Performance for Histogram-based and accessible Feature

Table 16: Comparison of model performance for histogram-based and accessible features

Window Width		10 EFC		25 EFC		50 EFC		100 EFC	
Model No.		H1	SF1	H2	SF2	H3	SF3	H4	SF4
Metrics									
R^2	Train	0.378	0.233	0.470	0.352	0.426	0.453	0.432	0.378
	Validation	0.291	0.169	0.385	0.335	0.357	0.436	0.481	0.392
	1. Test	0.266	0.188	0.384	0.307	0.343	0.365	0.289	0.431
	2. Test	0.212	0.182	0.313	0.304	0.264	0.202	0.382	0.308
	μ_{R^2}	0.287	0.193	0.388	0.325	0.347	0.364	0.396	0.377
	σ_{R^2}	0.059	0.024	0.055	0.019	0.057	0.099	0.070	0.044
RMSE	Train	0.923	1.025	1.209	1.336	1.461	1.402	1.585	1.607
	Validation	1.011	1.094	1.287	1.338	1.460	1.444	1.531	1.605
	1. Test	1.055	1.109	1.189	1.261	1.582	1.491	1.550	1.482
	2. Test	1.044	1.064	1.285	1.293	1.485	1.496	1.466	1.459
	μ_{RMSE}	1.008	1.073	1.242	1.307	1.497	1.458	1.533	1.538
	σ_{RMSE}	0.051	0.032	0.043	0.032	0.050	0.038	0.043	0.068